

# Calorimetry at a Future Linear Collider

Steven Green  
of Emmanuel College

A dissertation submitted to the University of Cambridge  
for the degree of Doctor of Philosophy



# Abstract

This thesis describes the optimisation of the calorimeter design for collider experiments at the future Compact Linear Collider (CLIC) and the International Linear Collider (ILC). The detector design of these experiments is built around high-granularity Particle Flow Calorimetry that, in contrast to traditional calorimetry, uses the energy measurements for charged particles from the tracking detectors. This can only be realised if calorimetric energy deposits from charged particles can be separated from those of neutral particles. This is made possible with fine granularity calorimeters and sophisticated pattern recognition software, which is provided by the PandoraPFA algorithm. This thesis presents results on Particle Flow calorimetry performance for a number of detector configurations. To obtain these results a new calibration procedure was developed and applied to the detector simulation and reconstruction to ensure optimal performance was achieved for each detector configuration considered.

This thesis also describes the development of a software compensation technique that vastly improves the intrinsic energy resolution of a Particle Flow Calorimetry detector. This technique is implemented within the PandoraPFA framework and demonstrates the gains that can be made by fully exploiting the information provided by the fine granularity calorimeters envisaged at a future linear collider.

A study of the sensitivity of the CLIC experiment to anomalous gauge couplings that effect vector boson scattering processes is presented. These anomalous couplings provide insight into possible beyond standard model physics. This study, which utilises the excellent jet energy resolution from Particle Flow Calorimetry, was performed at centre-of-mass energies of 1.4 TeV and 3 TeV with integrated luminosities of  $1.5\text{ab}^{-1}$

and  $2\text{ab}^{-1}$  respectively. The precision achievable at CLIC is shown to be approximately one to two orders of magnitude better than that currently offered by the LHC.

In addition, a study into various technology options for the CLIC vertex detector is described.

## Declaration

This dissertation is the result of my own work, except where explicit reference is made to the work of others, and has not been submitted for another qualification to this or any other university. This dissertation does not exceed the word limit for the respective Degree Committee.

Steven Green



## Acknowledgements

Of the many people who deserve thanks, some are particularly prominent, such as my supervisor. . .





# Contents

<b>1</b>	<b>Anomalous Gauge Coupling Theory</b>	<b>1</b>
1.1	The Standard Model . . . . .	1
1.2	Higgs Physics . . . . .	5
1.2.1	Spontaneous Symmetry Breaking . . . . .	5
1.2.2	Electroweak Interactions . . . . .	6
1.2.2.1	Custodial Symmetry . . . . .	8
1.3	Effective Field Theory . . . . .	10
1.4	Electroweak Chiral Lagrangian . . . . .	11
<b>2</b>	<b>The Sensitivity of CLIC to Anomalous Gauge Couplings through Vector Boson Scattering</b>	<b>15</b>
2.1	Motivation . . . . .	15
2.2	Event Generation, Simulation and Reconstruction . . . . .	19
2.3	Modelling of Anomalous Gauge Couplings . . . . .	21
2.4	Data Analysis . . . . .	24
2.4.1	Limiting Beam Related Backgrounds . . . . .	24
2.4.2	Jet Finding . . . . .	24
2.4.2.1	Optimal Jet Finding Algorithm . . . . .	27
2.4.3	Lepton Finding . . . . .	29
2.4.4	Discriminant Variables . . . . .	29
2.4.5	Jet Energy Resolution at CLIC . . . . .	30
2.5	Event Selection . . . . .	31
2.5.1	Preselection . . . . .	32
2.5.2	Multivariate analysis . . . . .	32
2.5.3	Event Selection Summary . . . . .	36
2.6	Anomalous Coupling Fitting Methodology . . . . .	36
2.6.1	Sensitive Distribution . . . . .	36
2.6.2	$\chi^2$ Surface and Confidence Limit Definition . . . . .	39

2.6.3	Event Weight Interpolation Scheme . . . . .	41
2.7	Results . . . . .	42
2.7.1	Systematic Uncertainties . . . . .	42
2.8	Sensitivity for $\sqrt{s} = 3$ TeV . . . . .	46
	<b>Bibliography</b>	<b>55</b>

*“Writing in English is the most ingenious torture  
ever devised for sins committed in previous lives.”*

— James Joyce



# Chapter 1

## Anomalous Gauge Coupling Theory

*"Meaningless! Meaningless!" says the Teacher. "Utterly meaningless! Everything is meaningless."*

— Ecclesiastes 1:2

Presented in chapter 2 is an analysis of the sensitivity of the CLIC experiment to the anomalous gauge couplings  $\alpha_4$  and  $\alpha_5$  through the vector boson scattering process. Here a brief description of the Standard Model of particle physics and a deeper discussion of the anomalous coupling theory studied in chapter 2 is given.

### 1.1 The Standard Model

The Standard Model is a non-abelian gauge theory of the  $SU(3) \times SU(2)_L \times U(1)$  symmetry group. It provides a description of three of the four fundamental forces of nature: the electromagnetic, weak and strong nuclear forces [1, 2]. The Standard Model contains a total of 24 fermion fields: six flavours of quark, each with three colours, and six leptons. A summary of the properties of these particles is given in table 1.1 and 1.2. As these fields,  $\psi$ , are spin- $\frac{1}{2}$ , they obey the Dirac equation

$$\mathcal{L} = \bar{\psi}(i\rlap{\not{D}} - m)\psi , \quad (1.1)$$

where  $\mathcal{L}$  is the Lagrangian density and  $m$  is a mass term. The derivative term,  $\rlap{\not{D}} = \gamma^\mu \partial_\mu$ , represents a summation over the partial derivate,  $\partial^\mu = (\frac{\partial}{\partial t}, \frac{\partial}{\partial x}, \frac{\partial}{\partial y}, \frac{\partial}{\partial z})$ , of the field  $\psi$  and the gamma matrices,  $\gamma^\mu$ . Each of the gauge transformations of the Standard Model are

defined by a unitary operator  $U$ , which acts to transform the vector space,  $\Psi$ , formed from a combination of fermion fields,  $\psi$ , in the following way

$$\Psi \rightarrow \Psi' = U\Psi . \quad (1.2)$$

In the Standard Model, the Lagrangian density describing the fermion fields is invariant

Generation	Particle	Mass [MeV]	Spin	Q/e
1	$e^-$	$0.548579909070 \pm 0.000000000016$	1/2	-1
	$\nu_e$	-	1/2	0
2	$\mu^-$	$105.6583745 \pm 0.0000024$	1/2	-1
	$\nu_\mu$	-	1/2	0
3	$\tau^-$	$1776.86 \pm 0.12$	1/2	-1
	$\nu_\tau$	-	1/2	0

**Table 1.1:** The mass, spin and electric charge (Q) of the leptons found in the Standard Model [3]. Neutrino masses have not been included in the above table as precise measurements are yet to be made. However, oscillations between different neutrino flavour states have been observed, which indicates that the flavour and mass eigenstates differ and that the neutrinos have a non-zero mass. The current upper bound on neutrino mass measurements is 2 eV.

Generation	Particle	Mass [MeV]	Spin	Q/e
1	$u$	$2.2^{+0.6}_{-0.4}$	1/2	+2/3
	$d$	$4.7^{+0.5}_{-0.4}$	1/2	-1/3
2	$c$	$1270 \pm 30$	1/2	+2/3
	$s$	$98^{+8}_{-4}$	1/2	+2/3
3	$t$	$173210 \pm 510 \pm 710$	1/2	+2/3
	$b$	$4180^{+40}_{-30}$	1/2	-1/3

**Table 1.2:** The mass, spin and electric charge (Q) of the quarks found in the Standard Model [3]. Each of the particles in the above table corresponds to three fermion fields, one for each of the three colours of the SU(3) symmetry.

under a SU(3), SU(2)<sub>L</sub> and U(1) gauge transformations. The SU(2)<sub>L</sub> gauge symmetry acts on doublets formed of pairs of left handed chiral components of the fermion fields,  $\psi_L = \frac{1}{2}(1 - \gamma_5)\psi$ , while the right handed components,  $\psi_R = \frac{1}{2}(1 + \gamma_5)\psi$ , transform

trivially as singlets [4]. Similarly, the SU(3) symmetry acts on triplets formed of the fermion fields for each flavour of quark. All fields transform under the fundamental representation of U(1). The invariance of the Standard Model Lagrangian to these gauge transformations is established by introducing 12 gauge fields, summarised in table 1.3, through the covariant derivate of the fermion fields

$$\partial^\mu \rightarrow D^\mu = \partial^\mu + ig_1 Y B^\mu + ig_2 \mathbf{T} \cdot \mathbf{W}^\mu + ig_3 \mathbf{X} \cdot \mathbf{G}^\mu , \quad (1.3)$$

where  $B^\mu$  is the gauge field for the U(1) symmetry,  $\mathbf{W}^\mu$  ( $W_j^\mu, j = 1, 2, 3$ ) are the fields of the SU(2)<sub>L</sub> symmetry and  $\mathbf{G}^\mu$  ( $G_j^\mu, j = 1, \dots, 8$ ) are the fields of the SU(3).  $Y$  is the weak hypercharge, which relates to the chirality and flavour of the fermion field that it is associated to. The three coefficients  $g_1$ ,  $g_2$  and  $g_3$  are coupling constants related to the three gauged symmetry groups in the Standard Model. Mixing of the gauge fields for the U(1) and SU(2) symmetry of the form

$$Z_\mu = \cos\theta_W W_\mu^3 - \sin\theta_W B_\mu , \quad (1.4)$$

$$A_\mu = \sin\theta_W W_\mu^3 + \cos\theta_W B_\mu , \quad (1.5)$$

$$W_\mu^\pm = \frac{1}{\sqrt{2}}(W_\mu^1 \mp iW_\mu^2) , \quad (1.6)$$

where

$$\cos\theta_W = \frac{g_2}{g_1 + g_2} \text{ and } \sin\theta_W = \frac{g_1}{g_1 + g_2} , \quad (1.7)$$

gives the electroweak gauge bosons;  $W^\pm$ ,  $Z$  and  $\gamma$ . This mixing ensures that the  $W^\pm$  and  $Z$  bosons become massive, while the  $\gamma$  remains massless. The  $G_j^\mu$  fields are the eight massless gluons of the strong force.  $\mathbf{T}$  and  $\mathbf{X}$  are the generators for the SU(2) and SU(3) symmetries, which are typically chosen as

$$T_i = \frac{1}{2}\tau_i , \quad (1.8)$$

$$X_i = \frac{1}{2}\lambda_i , \quad (1.9)$$

$$(1.10)$$

where  $\tau$  and  $\lambda$  are the Pauli and the Gell-Mann matrices respectively. The gauge fields

Force	Particle	Mass [GeV]	Spin	Q/e
Electromagnetic	$\gamma$	0	1	0
Weak Nuclear	$W^\pm$	$80.385 \pm 0.015$	1	$\pm 1$
	Z	$91.1876 \pm 0.0021$	1	0
Strong Nuclear	$g$ ( $\times 8$ colours)	0	1	0
Higgs	H	$125.1 \pm 0.3$	0	0

**Table 1.3:** The mass, spin and electric charge (Q) of the gauge bosons found in the Standard Model [3]. The  $\gamma$  and  $gs$  theoretically have zero mass, which is consistent with measurements. The upper bound on the  $\gamma$  mass has been measured at  $10^{-18}$  eV, while gluon masses of up to a few MeV have not been precluded. The upper bound on the magnitude of the charge of the  $\gamma$  is measured at  $10^{-35}$ .

of the Standard Model,  $B_\mu$ ,  $\mathbf{W}_\mu$  and  $\mathbf{G}_\mu$ , transform under the gauge transformations as

$$K_\mu \rightarrow K'_\mu = UK_\mu U^\dagger + \frac{i}{g}(\partial^\mu U)U^\dagger, \quad (1.11)$$

where  $K_\mu$  is any of  $B_\mu$ ,  $\mathbf{W}_\mu$  and  $\mathbf{G}_\mu$  and  $g$  is the coupling constants associated to the relevant gauged symmetry group. As the  $B_\mu$ ,  $\mathbf{W}_\mu$  and  $\mathbf{G}_\mu$  gauge fields are spin-1, they are described by the Proca Lagrangian density

$$\mathcal{L} = -\frac{1}{4}F_i^{\mu\nu}F_{\mu\nu} + \frac{1}{2}m_K^2 K_{i\mu}K_i^\mu, \quad (1.12)$$

where

$$F_i^{\mu\nu} = \partial^\mu K_i^\nu - \partial^\nu K_i^\mu - gf_{ijk}K_j^\mu K_k^\nu, \quad (1.13)$$

$f_{ijk}$  are the fully anti-symmetric structure constants of the group,  $K_i^\mu$  is the  $i^{th}$  gauge field of the group and  $m_K$  is a mass term for the gauge boson. The structure constants are defined from the commutation relations between generators of the symmetry group

$$[T_i, T_j] = if_{ijk}T_k. \quad (1.14)$$

These structure constants govern the self-interactions for the gauge bosons. There is only one structure constant for the U(1) symmetry, which is zero, as the U(1) symmetry is abelian. The SU(2) symmetry structure constants are  $f_{ijk} = \epsilon_{ijk}$ , where  $\epsilon_{ijk}$  is the Levi-Civita tensor. Due to the symmetries that are present in the Standard Model,  $m_K = 0$  for all the gauge fields, however, it is clear that is is not the case. Therefore, to



generate gauge boson mass terms a Higgs field is introduced that undergoes spontaneous symmetry breaking, as described in section 1.2.

## 1.2 Higgs Physics

Mass terms are generated in the Standard Model by introducing a Higgs field that undergoes spontaneous symmetry breaking. This allows the gauge bosons, as well as the quarks and leptons, to obtain a mass, while still respecting the gauge symmetries found in the Standard Model.

### 1.2.1 Spontaneous Symmetry Breaking

To illustrate spontaneous symmetry breaking, consider a complex scalar field  $\psi$  with the Klein-Gordon Lagrangian

$$\mathcal{L} = \partial^\mu \psi^* \partial_\mu \psi - m^2 |\psi|^2 = \partial^\mu \psi^* \partial_\mu \psi - V(\psi) , \quad (1.15)$$

where  $m$  is a mass term and  $V(\psi)$  is the potential the field  $\psi$ . This Lagrangian density is invariant under the global symmetry  $\psi \rightarrow e^{i\alpha} \psi$ . By adding extra terms to the Lagrangian, which retain the invariance to this global symmetry, it is possible to modify the interactions of this scalar field. For example, consider modifying the potential of the scalar field to the following

$$V(\psi) = m^2 |\psi|^2 + \lambda |\psi|^4 , \quad (1.16)$$

If  $m^2 > 0$ , the potential has a minima at zero, however, if  $m^2 < 0$  then the minima exists on a circle in the complex  $\psi$  plane, which is centred at  $(0, 0)$  and has radius  $v = \sqrt{-m^2/\lambda}$ . To quantise this theory it is necessary to expand about the minima of the potential. However, in the case of  $m^2 < 0$  there are an infinite number of choices of minima to expand about. Irrespective of the choice of minima used to expand the field about, the symmetry  $\psi \rightarrow e^{i\alpha} \psi$  is broken. Fluctuations about the minima along the degenerate direction leave the potential unchanged, which is a consequence of the breaking of the  $\psi \rightarrow e^{i\alpha} \psi$  symmetry; this is known as spontaneous symmetry breaking. Goldstone's theorem [5] implies that, for Lorentz-invariant theories, spontaneous symmetry breaking always leads to the existence a massless particles known as Goldstone bosons. For

example, consider expanding the complex scalar  $\psi$  about the minima. In that case,  $\psi$  takes the form

$$\psi = \frac{1}{\sqrt{2}}(v + \psi_1 + i\psi_2) , \quad (1.17)$$

where  $\psi_1$  and  $\psi_2$  are real fields and  $v = \sqrt{-m^2/\lambda}$ . Applying this parameterisation to the Lagrangian yields a mass term of  $\sqrt{-m^2}$  for the  $\psi_1$  field. However, there is no corresponding mass term for the  $\psi_2$  field, which indicates that it is massless as predicated by Goldstone's theorem

$$\mathcal{L} = \frac{1}{2}\partial^\mu\psi_1\partial_\mu\psi_1 + \frac{1}{2}\partial^\mu\psi_2\partial_\mu\psi_2 - m^2|\psi_1|^2 + \dots , \quad (1.18)$$

Spontaneous symmetry breaking is the origin of the gauge boson mass terms when applied to local symmetries instead of global ones. For example consider the global symmetry,  $\psi \rightarrow e^{i\alpha}\psi$  that exists in equation 1.15. If this global symmetry is promoted to a local symmetry by letting  $\alpha \rightarrow \alpha(x)$  and  $\partial^\mu \rightarrow D^\mu = \partial^\mu + iA^\mu$ , where  $A^\mu$  a the gauge field that transforms as  $A^\mu \rightarrow A^\mu - \partial^\mu\alpha(x)$ , the Lagrangian becomes

$$\mathcal{L} = (D^\mu\psi)^*(D_\mu\psi) - m^2|\psi|^2 - \lambda|\psi|^4 . \quad (1.19)$$

If the  $\psi$  field is expanded about a non-zero minima in the potential, i.e.  $m^2 < 0$  and  $v = \sqrt{-m^2/\lambda}$ , as was done in equation 1.17, then a gauge boson mass term,  $+\frac{v^2}{2}A^\mu A_\mu$ , is generated from the  $(D^\mu\psi)^*(D_\mu\psi)$  term.

## 1.2.2 Electroweak Interactions

The electroweak sector of the Standard Model is that related to the  $SU(2)_L \times U(1)$  symmetry [6]. In this sector, spontaneous symmetry breaking must occur in such a way as to give three massive gauge bosons,  $W^\pm$  and  $Z$ , and one massless gauge boson, the  $\gamma$ . This can be achieved through a Higgs field,  $H$ , that transforms as a doublet under the  $SU(2)_L$  symmetry. The Lagrangian for this field is

$$\mathcal{L}_{Higgs} = (D_\mu H)^\dagger D^\mu H - V(H) . \quad (1.20)$$

The Higgs potential,  $V(H)$ , is

$$V(H) = -\mu^2 H^\dagger H + \lambda (H^\dagger H)^2 , \quad (1.21)$$

where  $\mu$  and  $\lambda$  are constants. The covariant derivative of this Higgs field must satisfy the  $SU(2)_L \times U(1)$  gauge symmetry meaning it takes the form

$$D_\mu H = (\partial_\mu + ig_1 Y B_\mu + ig_2 \frac{\tau^i}{2} W_\mu^i) H , \quad (1.22)$$

where  $g_1$  and  $g_2$  are coupling constants for the  $U(1)$  and  $SU(2)_L$  gauged symmetries respectively,  $Y = \frac{1}{2}$  is the weak hypercharge of the Higgs and  $\tau^i$  are the Pauli matrices.  $B_\mu$  and  $W_\mu^i$  are the gauge fields for the  $U(1)$  and  $SU(2)_L$  gauged symmetries respectively.

Consider spontaneously breaking the symmetry in the Higgs sector by expanding the Higgs field about a non-zero vacuum expectation value (vev)

$$\langle H \rangle = \begin{pmatrix} 0 \\ \frac{v}{\sqrt{2}} \end{pmatrix} , \quad (1.23)$$

where the minima of the field is defined as

$$\frac{v}{\sqrt{2}} = \sqrt{\frac{\mu^2}{2\lambda}} , \quad (1.24)$$

where  $v$  real. In that case, the kinematic term in the Higgs Lagrangian,  $D^\mu H^\dagger D_\mu H$ , contains mass terms for the gauge bosons

$$D^\mu H^\dagger D_\mu H \supset \frac{v^2}{2} (ig_1 Y B^\mu + ig_2 \frac{\tau^i}{2} W^{i\mu}) (ig_1 Y B_\mu + ig_2 \frac{\tau^i}{2} W_\mu^i) . \quad (1.25)$$

If there is mixing of the  $SU(2)_L$  and  $U(1)$  fields of the form

$$Z_\mu = \cos\theta_W W_\mu^3 - \sin\theta_W B_\mu , \quad (1.26)$$

$$A_\mu = \sin\theta_W W_\mu^3 + \cos\theta_W B_\mu , \quad (1.27)$$

$$W_\mu^\pm = \frac{1}{\sqrt{2}} (W_\mu^1 \mp i W_\mu^2) , \quad (1.28)$$

then the following gauge boson mass terms are generated

$$\frac{(gv)^2}{4} W_\mu^+ W^{-\mu} + \frac{(g^2 + g'^2)v^2}{8} Z_\mu Z^\mu . \quad (1.29)$$

The gauge boson masses generated by spontaneous symmetry breaking of the Higgs field are

$$\begin{aligned} m_W &= \frac{gv}{2} , \\ m_Z &= \frac{v\sqrt{g^2 + g'^2}}{2} = \frac{m_W}{\cos\theta_W} , \\ m_A &= 0 , \end{aligned} \tag{1.30}$$

where  $\theta_W$  is the Weinberg angle. This mixing produces a massless gauge boson, the  $\gamma$ , and three massive gauge bosons, the  $W^\pm$  and  $Z$ . By acquiring a non-zero vev, the Higgs field breaks the  $SU(2)_L \times U(1)$  symmetry that was present in the Lagrangian to the  $U(1)_{em}$  symmetry of electromagnetism.

The ratio of the masses of the  $W^\pm$  and  $Z$  bosons is predicted when spontaneous symmetry breaking occurs in the Higgs sector. This prediction sets the  $\rho$  parameter to unity, where the  $\rho$  parameter is defined as

$$\rho = \frac{m_W^2}{m_Z^2 \cos^2\theta_W} = 1 . \tag{1.31}$$

This is a consequence of the Higgs potential containing custodial symmetry [3]. As the  $\rho$  parameter has been experimentally measured to be  $1.00040 \pm 0.00024$  [7], it is clear that any extension to the Standard Model should retain this result.

### 1.2.2.1 Custodial Symmetry

The Standard Model Higgs field is defined by the Lagrangian

$$\mathcal{L}_{Higgs} = (D_\mu H)^\dagger D^\mu H - V(H), \tag{1.32}$$

where

$$V(H) = -\mu^2 H^\dagger H + \lambda (H^\dagger H)^2 , \tag{1.33}$$

and  $\mu$  and  $\lambda$  are constants. By construction, the Higgs sector of the Standard Model is invariant under local  $SU(2)_L \times U(1)$  gauge transformations. However, a larger global

symmetry also exists in this sector, which can be seen by considering the Higgs doublet [8]

$$H = \begin{pmatrix} \psi^+ \\ \psi^0 \end{pmatrix} = \begin{pmatrix} \psi_1 + i\psi_2 \\ \psi_3 + i\psi_4 \end{pmatrix}. \quad (1.34)$$

All the terms in the Higgs potential involve  $H^\dagger H = \psi_1^2 + \psi_2^2 + \psi_3^2 + \psi_4^2$ , which is invariant under any rotation of these four components and hence under a  $SO(4)$  global symmetry. In general,  $SO(4) \cong SU(2) \times SU(2)$ , where  $\cong$  denotes an isomorphism. In the case of the Higgs sector  $SO(4) \cong SU(2)_L \times SU(2)_R$  where the  $SU(2)_L$  symmetry is the gauged symmetry of the Standard Model. This symmetry can be manifested using an alternative parameterisation [9] of the Higgs field

$$\Phi = (i\tau_2 H, H) = \begin{pmatrix} \psi^{0*} & \psi^+ \\ -\psi^{+*} & \psi^0 \end{pmatrix}. \quad (1.35)$$

In this parametrisation the Higgs Lagrangian,  $\mathcal{L}_{Higgs}$ , becomes

$$\mathcal{L}_{Higgs} = \frac{1}{2} \text{Tr}[(D_\mu \Phi)^\dagger D^\mu \Phi] + \mu^2 \text{Tr}[\Phi^\dagger \Phi] - \lambda \text{Tr}[\Phi^\dagger \Phi \Phi^\dagger \Phi], \quad (1.36)$$

which is invariant under transformations of the form

$$\Phi \rightarrow U_L \Phi U_R^\dagger, \quad (1.37)$$

where  $U_L$  and  $U_R$  are transformations of the  $SU(2)_L$  and  $SU(2)_R$  symmetry groups respectively.

When the Higgs field acquires a non-zero vev the  $SU(2)_L \times SU(2)_R$  symmetry of the Higgs potential is broken to a  $SU(2)_C$  symmetry, which is known as custodial symmetry [10]. As  $SO(3) \cong SU(2)$ , symmetry breaking in the Higgs sector is equivalent to a  $SO(4)$  symmetry being broken to a  $SO(3)$  symmetry. This becomes clear when considering the form of the Higgs potential after symmetry breaking. Prior to symmetry breaking a  $SO(4)$  global symmetry is present, however, after expanding the Higgs about a non-zero vev, defined in equation 1.23, the terms in the Higgs potential involve  $H^\dagger H = (\psi_3 - v)^2 + \psi_1^2 + \psi_2^2 + \psi_4^2$ , which is only invariant to rotations between the  $\psi_1$ ,  $\psi_2$  and  $\psi_4$  fields, which is a  $SO(3)$  symmetry.

The Higgs field,  $H$ , transforms a singlet under this  $SU(2)_C$  custodial symmetry, while the  $SU(2)_L$  gauge boson fields,  $W_\mu^i$ , transform as a triplet. It is the transformation of the

$W_\mu^i$  fields under the  $SU(2)_C$  symmetry that enforces the relationship between the masses of the  $W^\pm$  and  $Z$  gauge bosons and that  $\rho$  should equal unity. It should be noted that the  $SU(2)_L \times SU(2)_R$  symmetry only exists in the Higgs sector of the Standard Model. The  $SU(2)_R$  symmetry in the Standard Model is broken by Yukawa couplings of the Higgs to quarks and leptons and by a non-zero coupling to the  $U(1)$  gauge symmetry of the Standard Model,  $g_1$ . However, this breaking of the  $SU(2)_R$  symmetry is weak, which means the deviations of  $\rho$  from unity are minimal [10].

### 1.3 Effective Field Theory

There are a number of features in the observable universe that cannot be accounted for using the Standard Model of particle physics. However, the Standard Model is a very good description of the interactions between particles at the energies being probed at modern particle collider experiments. Any underlying theory governing the interactions of particles must, therefore, behave like the Standard Model over these energies, or distance scales. Above such energies the theory will deviate from the Standard Model to account for the full underlying theory. Effective field theories (EFTs) work from this premise by assuming that the complete theory has a momentum scale,  $\Lambda$ , below which Standard Model behaviour is replicated [11, 12].

Quantum field theories must be renormalizable to ensure that non-infinite predictions of the coefficients in the Lagrangian can be made and tested [13]. Infinities arise from non-renormalizable theories due to divergent integrals from loop diagrams that assume the theory being applied is valid at all energy and length scales. Effective field theories act to avoid such problems by only integrating up to the momentum scale  $\Lambda$  and not above it. At the energy scale being considered, any infinities arising from the loop calculations in the EFT can be absorbed into a finite number of parameters. This methodology avoids the assumption that the theory in question is applicable to all energy scales and allows measurable predictions to be made.

As the Standard Model should be replicated at the low energy scale, it is appropriate when creating an EFT Lagrangian to append new operators to the Standard Model Lagrangian to account for areas of new physics. This gives the general form for an EFT

Lagrangian as [11]

$$\mathcal{L}_{EFT} = \mathcal{L}_{SM} + \sum_{\text{dimension } d > 4} \sum_i \frac{c_i^{(d)}}{\Lambda^{d-4}} \mathcal{O}_i^{(d)}, \quad (1.38)$$

where  $\mathcal{L}_{SM}$  is the Standard Model Lagrangian,  $c_i^{(d)}$  are free parameters,  $\mathcal{O}_i^{(d)}$  is the  $i^{th}$  unique operator with dimension  $d$  in the EFT and  $\Lambda$  is the EFT momentum scale. The sum runs over all unique operators with dimension greater than four. The presence of the  $\Lambda^{d-4}$  in the denominator is required to ensure correct dimensionality of the new terms being added to the Lagrangian.

New physics is introduced by the operators  $\mathcal{O}_i^{(d)}$ , but suppressed by the momentum scale  $\Lambda$ . It is assumed that  $\Lambda$  is large with respect to the momentum scales that have been examined at preexisting particle collider experiments, therefore, any new physics is suppressed. Under this assumption, new operators with dimension less than, or equal to, four can be vetoed from the EFT as their effects would be readily observed at preexisting particle collider experiments, due to the  $\Lambda^{4-d}$  coefficient. At energies below the momentum scale,  $\Lambda$ , it is possible to find the dominant new physics terms in the EFT and consider these as corrections to the Standard Model. Above this scale the EFT breaks down as operator  $\mathcal{O}_i^{(d)}$  in  $\mathcal{L}_{EFT}$  has a non-negligible coefficient. In the extremal limit,  $\Lambda \rightarrow \infty$ , the Standard Model is recovered as new physics is too far out of reach to have any impact on observables.

## 1.4 Electroweak Chiral Lagrangian

The introduction of a Higgs field undergoing spontaneous symmetry breaking is able to produce mass terms in the Lagrangian for the  $W^\pm$  and  $Z$  bosons. However, it is possible to introduce these terms by parameterising the Higgs field using the gauge boson fields of the  $SU(2)_L$  Standard Model symmetry [14]. In this approach, the pattern of spontaneous symmetry breaking mirrors that found in the Higgs sector of the Standard Model i.e. a global  $SU(2)_L \times SU(2)_R$  symmetry is broken to a  $SU(2)_C$  symmetry. This will ensure that the  $\rho$  parameter, introduced in section 1.2.2, retains a value of unity, which is consistent with experimental measurements. The Standard Model spontaneous symmetry breaking pattern can be replicated using a field,  $\Sigma(x)$ , which transforms under

the  $SU(2)_L \times SU(2)_R$  global symmetries as

$$\Sigma \rightarrow U_L \Sigma U_R^\dagger, \quad (1.39)$$

where  $U_L$  and  $U_R$  are transformations of the  $SU(2)_L$  and  $SU(2)_R$  symmetry groups respectively and  $\Sigma(x)$  is

$$\Sigma(x) = \exp\left(\frac{-i}{v} \Sigma_{a=1}^3 \pi^a \tau^a\right), \quad (1.40)$$

where  $\pi^a$  are the three would-be Goldstone bosons that exist when the  $SU(2)_L \times U(1)$  symmetry is broken to  $U(1)_{em}$  [15]. The  $SU(2)_L$  and  $U(1)$  symmetries of the Standard Model are gauged in the usual way by defining the covariant derivate of the  $\Sigma$  field

$$\mathcal{D}_\mu \Sigma(x) = \partial_\mu \Sigma(x) + \frac{ig_2}{2} W_\mu^a \tau^a \Sigma(x) - \frac{ig_1}{2} B_\mu \tau^3 \Sigma(x), \quad (1.41)$$

where  $g_1$  and  $g_2$  are coupling constants for the  $U(1)$  and  $SU(2)_L$  symmetries respectively and  $\tau^a$  are the Pauli spin matrices. The lowest order derivative term for this  $\Sigma$  field that could appear in the Lagrangian is

$$\mathcal{L}_\Sigma = \frac{v^2}{4} \text{Tr}(\mathcal{D}^\mu \Sigma^\dagger \mathcal{D}_\mu \Sigma) = -\frac{v^2}{4} \text{Tr}(V_\mu V^\mu), \quad (1.42)$$

where  $V_\mu = (\mathcal{D}_\mu \Sigma) \Sigma^\dagger$ . This terms respects all the symmetries present in the Higgs sector of that Standard Model, including the custodial symmetry in the limit  $g_1 \rightarrow 0$ . Furthermore, by expanding this field about a non-zero vev, the  $SU(2)_L \times SU(2)_R$  global symmetry is broken to a  $SU(2)_C$  symmetry exactly as it is in the Standard Model. For example, if this field is expanded about the point  $\Sigma = \mathbb{K}$ , i.e. the unitary gauge, mass terms for the electroweak gauge bosons are generated that match those produced from spontaneous symmetry breaking of the Higgs field as described in section 1.2.1

$$\frac{v^2}{4} \text{Tr}[V^\mu V_\mu] = -\frac{(gv)^2}{4} W_\mu^+ W^{-\mu} - \frac{(g^2 + g'^2)v^2}{8} Z_\mu Z^\mu \quad (1.43)$$

$$\begin{aligned} m_A &= 0, \\ m_W &= \frac{gv}{2}, \\ m_Z &= \frac{v\sqrt{g^2 + g'^2}}{2} = \frac{m_W}{\cos\theta_W}, \end{aligned} \quad (1.44)$$



So far, all that has been done is a parameterisation of the Higgs field, however, it was shown by Longhitano [15] that there are several relevant operators involving the  $\Sigma$  field that are  $SU(2)_L \times U(1)$  invariant. As these operators obey the same symmetries as those found in the Standard Model they should be considered. This can be done using EFT approach, as discussed in section 1.3. Of the operators introduced by Longhitano, only two involve quartic massive gauge boson vertices and preserve the custodial symmetry [16]. They are

$$\alpha_4 \text{Tr}[V^\mu V_\nu] \text{Tr}[V^\nu V_\mu] \quad \text{and} \quad \alpha_5 \text{Tr}[V^\mu V_\mu]^2. \quad (1.45)$$

These terms contribute to the massive gauge boson quartic vertices shown in figure 1.1. The Standard Model already contains triple and quartic vertices involving the electroweak gauge bosons, shown in figure 1.2, and these are also present in this EFT approach. These vertices originate from the kinematic terms in the Proca Lagrangian density  $\mathcal{L}_{kin} = -\frac{1}{4}B_{\mu\nu}B^{\mu\nu} - \frac{1}{4}W_{\mu\nu}W^{\mu\nu}$ . Of the vertices showing sensitivity to  $\alpha_4$  and  $\alpha_5$ , only that shown in figure 1.1c is not present in the Standard Model.

Both terms shown in equation 1.45 contain dimension 8 operators [11] and, with respect to the EFT approach, i.e. equation 1.38, their coefficients are proportional to  $\Lambda^{-4}$ , where  $\Lambda$  is the momentum scale of the new physics being modelled. In the limit that the momentum scale of new physics is beyond experimental reach, i.e.  $\Lambda \rightarrow \infty$ , these terms do not contribute to measurable observables and the Standard Model is recovered. It should be noted that in this case, the Standard Model has been parameterised using the  $\Sigma$  field, so in the limit  $\Lambda \rightarrow \infty$ , the gauge boson mass terms generated from  $\mathcal{L}_\Sigma$  do not vanish.

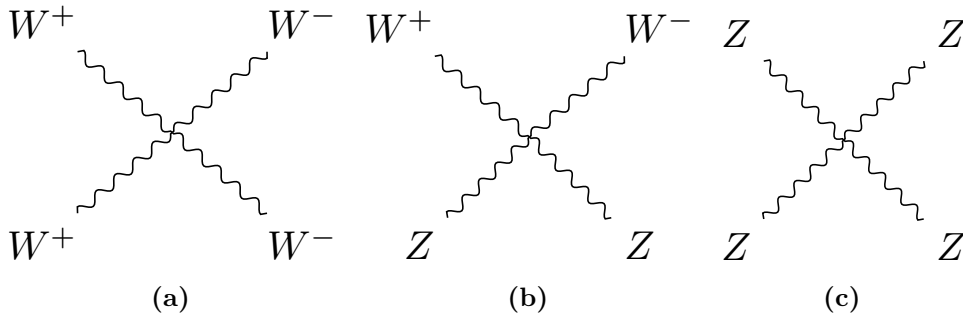


**Figure 1.1:** Gauge boson self-coupling vertices that are sensitive to the anomalous gauge couplings  $\alpha_4$  and  $\alpha_5$ .

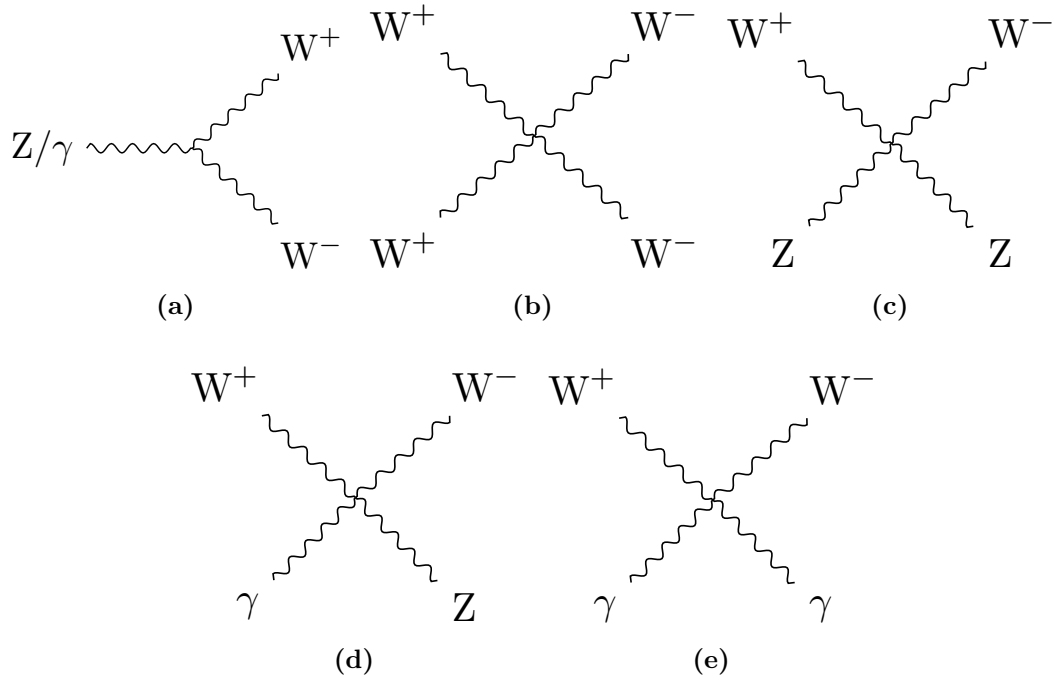


**Figure 1.2:** Gauge boson self-coupling vertices in the Standard Model.

## Chapter 2

# The Sensitivity of CLIC to Anomalous Gauge Couplings through Vector Boson Scattering

*“Kids, you tried your best, and you failed miserably. The lesson is, never try.”*

— Homer Simpson

### 2.1 Motivation

Vector boson scattering is the interaction of the form  $VV \rightarrow VV$  where  $V$  is any of the electroweak gauge bosons  $W^+$ ,  $W^-$ ,  $Z$  or  $\gamma$ . This is an interesting process to study because it provides understanding of how the Standard Model Higgs is able to unitarise the otherwise unbounded cross-section for longitudinal massive gauge boson scattering. Vector boson scattering also provides insights into beyond standard model physics that impacts the electroweak sector by probing potential anomalous triple and quartic gauge couplings.

Triple and quartic gauge couplings lead to interactions of the form  $V \rightarrow VV$  and  $VV \rightarrow VV$  respectively. In the Standard Model there are five allowed vertices, shown in figure 2.1, which arise from the kinematic term  $\mathcal{L}_{kin} = -\frac{1}{4}B_{\mu\nu}B^{\mu\nu} - \frac{1}{4}W_{\mu\nu}W^{\mu\nu}$  in the Standard Model Lagrangian.

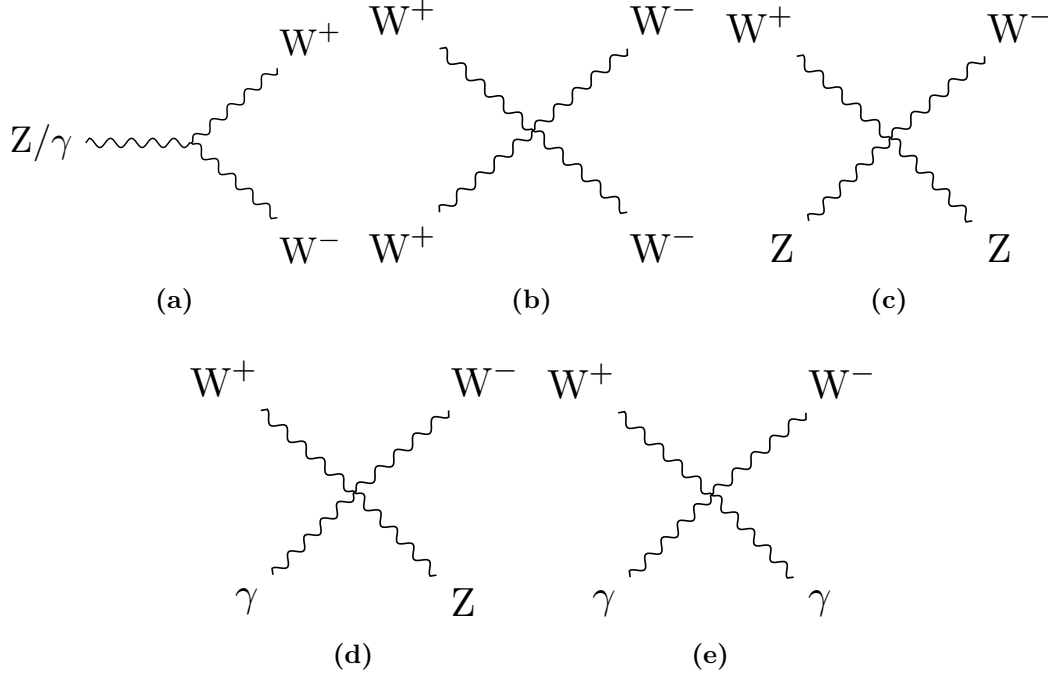


**Figure 2.1:** Triple and quartic gauge boson vertices in the Standard Model.

Anomalous triple and quartic gauge couplings are introduced as parameters in effective field theories (EFTs). These couplings either modify the Standard Model triple and quartic gauge boson vertices or introduce new triple and quartic vertices that were previously forbidden. EFTs are a mathematical construct designed to introduce new physics in a manner that builds upon the Standard Model. They work under the assumption that new physics exists at an energy scale,  $\Lambda$ , that is much higher than the energy scales currently accessible to modern day particle physics experiments. In the limit  $\Lambda \rightarrow \infty$ , the Standard Model is reproduced as the new physics becomes kinematically inaccessible. Such theories are model independent, giving them a wide span in the search for new physics. A classic example of an EFT theory is the Fermi theory for beta decay [17]. At energies much below the mass of the W boson, the weak interaction occurring when a neutron decays into a proton, electron and anti-neutrino can be treated as a four-point vertex with quartic coupling strength  $G_F$ , the Fermi Coupling constant as shown in figure 2.2.

The study presented in this chapter examines the anomalous quartic gauge couplings  $\alpha_4$  and  $\alpha_5$  through vector boson scattering process. The anomalous gauge couplings that are to be examined are introduced as part of an EFT that is described in chapter 1.

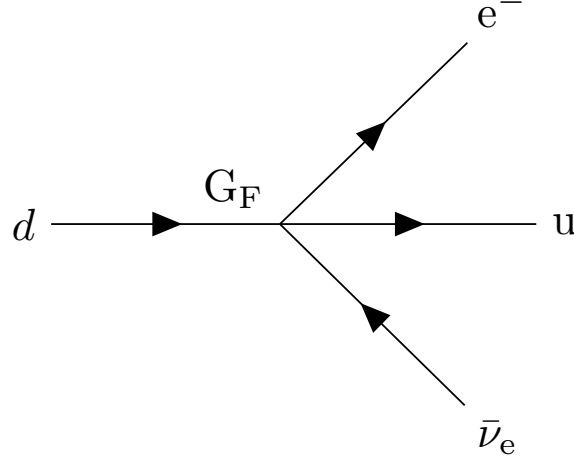


**Figure 2.2:** Four-point vertex proposed for explanation of beta decay by Fermi.

These couplings appear in the Lagrangian through the following terms

$$\alpha_4[\text{Tr}(V^\mu V_\mu)]^2 \quad \text{and} \quad \alpha_5 \text{Tr}(V^\mu V_\nu) \text{Tr}(V^\nu V_\mu) , \quad (2.1)$$

where  $V_\mu$  corresponds, in a carefully chosen gauge, to a linear combination of the massive gauge bosons  $W^+$ ,  $W^-$  and  $Z$ . These terms modify the Standard Model vertices  $W^+W^- \rightarrow W^+W^-$  and  $W^+W^- \rightarrow ZZ$  as well as introducing the new vertex  $ZZ \rightarrow ZZ$ . The anomalous gauge couplings  $\alpha_4$  and  $\alpha_5$  can be studied in vector boson scattering processes such as those shown in figure 2.3.

CLIC is designed for precision measurements in  $e^+e^-$  collisions at high energies and it is ideal for a study of vector boson scattering. The application of Particle Flow Calorimetry with fine granularity calorimeters gives CLIC excellent jet energy resolution, which allows it to clearly characterise multi-jet final states and final states containing missing energy in the form of neutrinos. The excellent jet energy resolution also allows for accurate separation of  $W$  and  $Z$  bosons through di-jet invariant mass, which will be invaluable for event selection.

The cross-sections for vector boson scattering processes are sufficiently large at the proposed running energies for CLIC to give large signal sample sizes. A study of anomalous gauge boson couplings at CLIC has the potential to give results several orders of magnitude better than the complementary studies performed at the LHC because of the reduction in hadronic backgrounds and increased cross-section for vector boson

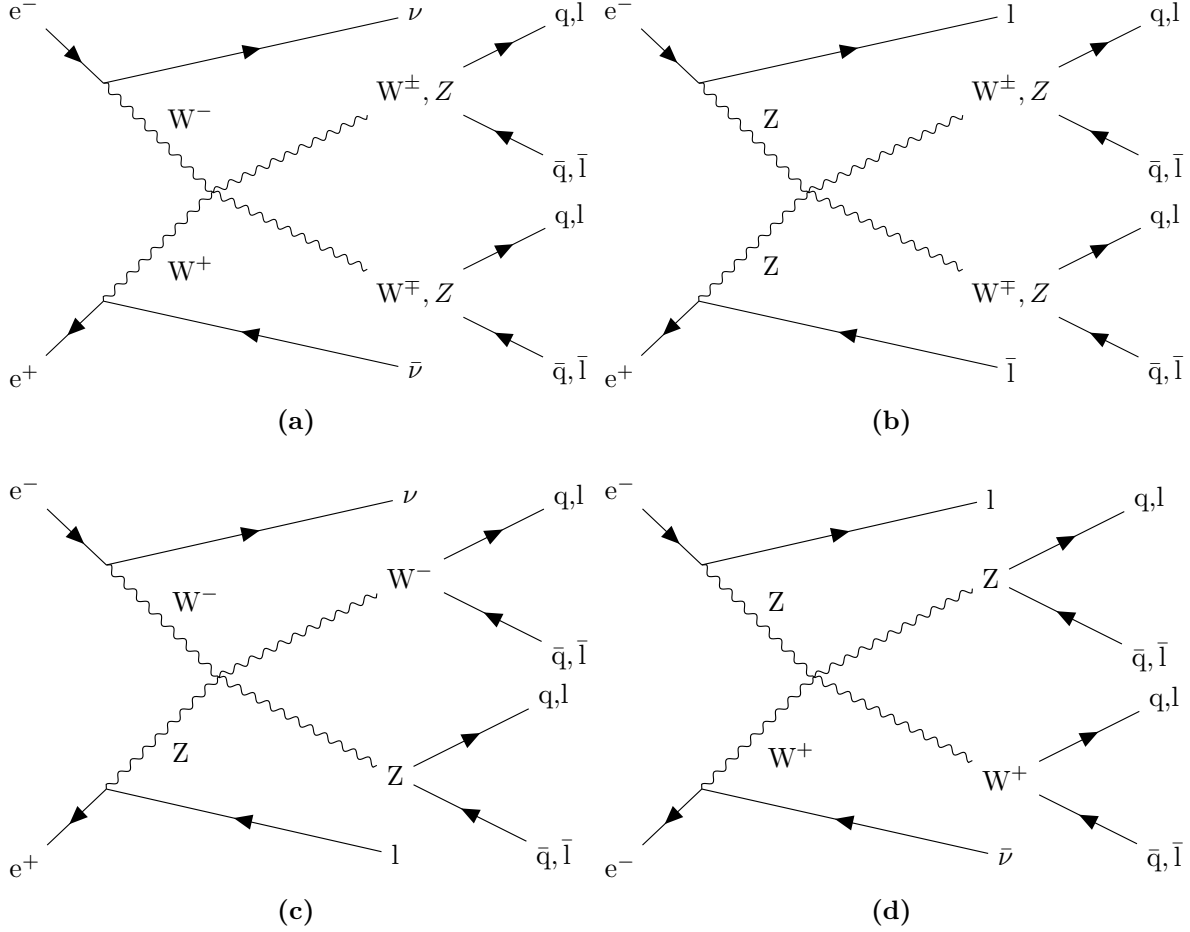


**Figure 2.3:** Example of vector boson scattering Feynman diagrams showing sensitivity to quartic gauge boson self-interaction vertices. The processes shown are relevant for CLIC. In these diagrams  $q$  represents the  $u, d, s, c$  and  $b$  quarks;  $l$  represents  $e^-, \mu^-$  and  $\tau^-$  leptons; and  $\nu$  represents the  $\nu_e, \nu_\mu$  and  $\nu_\tau$  neutrinos.

scattering processes [18]. The above reasons make a strong case for performing a vector boson scattering analysis at CLIC.

The branching fractions for the hadronic decays of both the  $W^\pm$  and  $Z$  bosons is of the order of 70% [3], therefore, the signal final states for the analysis presented in this chapter are vector boson scattering processes where the outgoing bosons decay purely hadronically:  $\nu\nu qqqq, \nu lqqqq$  and  $llqqqq$ .

## 2.2 Event Generation, Simulation and Reconstruction

Events were generated using Whizard [19, 20] version 1.95. Due to the presence of beamstrahlung photons in the CLIC beam, events were generated for collisions of  $e^+e^-$ ,  $e^+\gamma$ ,  $\gamma e^-$  and  $\gamma\gamma$ . The energy spectra used for all particles involved in these collisions took into account the effects of radiation in the form of beamstrahlung photons and the intrinsic energy spread of the CLIC beam. Furthermore, events involving the interaction between the electromagnetic field of the beam particles involving quasi-real photon mediators with low momenta, described by the Weizsacker-Williams approximation or the Equivalent Photon Approximation (EPA), were generated using Whizard and included in this analysis. Fragmentation and hadronisation was implemented using PYTHIA 6.4 [21] that was tuned for OPAL  $e^+e^-$  collision data recorded at LEP [22]. The decays of tau leptons was simulated using TAUOLA [23]. The full list of events used in this analysis, along with their Standard Model cross-section for  $\sqrt{s} = 1.4$  TeV can be found in table 2.1. The samples comprise all final states that are relevant, either as signal or background processes, for an analysis involving the purely hadronic decay channels from the vector boson scattering process:

- Final states from the purely hadronic decay channels of the vector boson scattering process. These states are expected to show sensitivity to the anomalous couplings  $\alpha_4$  and  $\alpha_5$ :  $e^+e^- \rightarrow \nu\nu qqqq$ ,  $e^+e^- \rightarrow \nu lqqqq$  and  $e^+e^- \rightarrow llqqqq$
- Final states with four primary quarks arising from  $e^+e^-$  interactions:  $e^+e^- \rightarrow qqqq$ .
- Final states with two primary quarks arising from  $e^+e^-$  interactions:  $e^+e^- \rightarrow \nu\nu qq$ ,  $e^+e^- \rightarrow \nu lqq$ ,  $e^+e^- \rightarrow llqq$  and  $e^+e^- \rightarrow qq$ .
- Final states with four primary quarks arising from the interactions of either  $e^+$  or  $e^-$  with a beamstrahlung photon:  $e^-\gamma_{BS} \rightarrow e^-qqqq$ ,  $e^+\gamma_{BS} \rightarrow e^+qqqq$ ,  $e^-\gamma_{BS} \rightarrow \nu_eqqqq$  and  $e^+\gamma_{BS} \rightarrow \bar{\nu}_eqqqq$ .
- Final states with four primary quarks arising from the interactions of either  $e^+$  or  $e^-$  with the electromagnetic field of the opposing beam particle. These cross-sections are calculated using the EPA approximation, which represents the electromagnetic field of the opposing beam particle as a series of photons, so the final states appear as interactions of  $e^+$  or  $e^-$  with photons:  $e^-\gamma_{EPA} \rightarrow e^-qqqq$ ,  $e^+\gamma_{EPA} \rightarrow e^+qqqq$ ,  $e^-\gamma_{EPA} \rightarrow \nu_eqqqq$  and  $e^+\gamma_{EPA} \rightarrow \bar{\nu}_eqqqq$ .

- Final states with four primary quarks arising from the interaction of the electromagnetic fields of opposing beam particles using the EPA approximation:  $\gamma_{\text{EPA}}\gamma_{\text{EPA}} \rightarrow q\bar{q}q\bar{q}$ .
- Final states with four primary quarks arising from the interaction of the electromagnetic field of either  $e^+$  or  $e^-$  using the EPA approximation with a beamstrahlung photon:  $\gamma_{\text{EPA}}\gamma_{\text{BS}} \rightarrow q\bar{q}q\bar{q}$  or  $\gamma_{\text{BS}}\gamma_{\text{EPA}} \rightarrow q\bar{q}q\bar{q}$ .
- Final states with four primary quarks arising from the interaction of two beamstrahlung photons:  $\gamma_{\text{BS}}\gamma_{\text{BS}} \rightarrow q\bar{q}q\bar{q}$ .

In the above list  $q$  represents  $u, \bar{u}, d, \bar{d}, s, \bar{s}, c, \bar{c}, b$  or  $\bar{b}$ ;  $l$  represents  $e^\pm, \mu^\pm$  or  $\tau^\pm$ ; and  $\nu$  represents  $\nu_e, \bar{\nu}_e, \nu_\mu, \bar{\nu}_\mu, \nu_\tau$  and  $\bar{\nu}_\tau$ .

Monte-Carlo (MC) samples were simulated using the CLID\_ILD detector model [24]. Further details of this detector model can be found in chapter ?? . The simulation was performed in MOKKA [25], which is a GEANT4 [26] wrapper providing detailed geometric descriptions of detector concepts for the linear collider. Events were reconstructed using the MARLIN [27] c++ framework, designed for reconstruction at the linear collider. PandoraPFA [28, 29] was used to apply Particle Flow Calorimetry in the reconstruction, the full details of which can be found in chapter ?? .

The effect of the  $\gamma\gamma \rightarrow \text{hadrons}$  backgrounds, discussed in section ?? , were incorporated in the analysis by overlaying  $\gamma\gamma \rightarrow \text{hadrons}$  events onto the signal and background event samples. The overlaid backgrounds were added prior to reconstruction so that their impact on the reconstruction was fully accounted for. For each physics event of interest,  $\gamma\gamma \rightarrow \text{hadrons}$  background events equivalent to 60 bunch crossings (BXs) are included. As readout time windows are applied in detector readout, 60 BXs is sufficient for accounting for the  $\gamma\gamma \rightarrow \text{hadrons}$  backgrounds. These backgrounds occur in a time window of  $-5$  ns to  $25$  ns around the physics event and the BXs are separated by  $0.5$  ns, to mimic the CLIC bunch train structure. The number of background events overlaid per BX is drawn from a Poisson distribution with a mean of  $1.3$  ( $3.2$ ) events per bunch crossing at  $\sqrt{s} = 1.4$  ( $3$ ) TeV [30].

Detector readout is simulated using a readout time window, of  $10$  ns on all detectors apart from the TPC and HCal barrel. All hits are kept in the TPC, while a  $100$  ns time window is used in the HCal barrel to account for the additional time it takes hadronic showers to develop in tungsten. All readout times are corrected for straight time-of-flight



Final State	Cross Section [fb]
$e^+e^- \rightarrow \nu\nu qqqq$	24.7
$e^+e^- \rightarrow \nu lqqqq$	110.4
$e^+e^- \rightarrow llqqqq$	62.1
$e^+e^- \rightarrow qqqq$	1245.1
$e^+e^- \rightarrow \nu\nu qq$	787.7
$e^+e^- \rightarrow \nu lqq$	4309.7
$e^+e^- \rightarrow llqq$	2725.8
$e^+e^- \rightarrow qq$	4009.5
$e^- \gamma_{\text{EPA}} \rightarrow e^- qqqq$	287.1
$e^- \gamma_{\text{BS}} \rightarrow e^- qqqq$	1160.7
$e^+ \gamma_{\text{EPA}} \rightarrow e^+ qqqq$	286.9
$e^+ \gamma_{\text{BS}} \rightarrow e^+ qqqq$	1156.3
$e^- \gamma_{\text{EPA}} \rightarrow \nu_e qqqq$	32.6
$e^- \gamma_{\text{BS}} \rightarrow \nu_e qqqq$	136.9
$e^+ \gamma_{\text{EPA}} \rightarrow \bar{\nu}_e qqqq$	32.6
$e^+ \gamma_{\text{BS}} \rightarrow \bar{\nu}_e qqqq$	136.4
$\gamma_{\text{EPA}} \gamma_{\text{EPA}} \rightarrow qqqq$	753.0
$\gamma_{\text{EPA}} \gamma_{\text{BS}} \rightarrow qqqq$	4034.8
$\gamma_{\text{BS}} \gamma_{\text{EPA}} \rightarrow qqqq$	4018.7
$\gamma_{\text{BS}} \gamma_{\text{BS}} \rightarrow qqqq$	21406.2

**Table 2.1:** Cross sections of signal and background processes for  $\sqrt{s} = 1.4$  TeV. In the above table q represents u,  $\bar{u}$ , d,  $\bar{d}$ , s,  $\bar{s}$ , c,  $\bar{c}$ , b or  $\bar{b}$ ; l represents  $e^\pm$ ,  $\mu^\pm$  or  $\tau^\pm$ ; and  $\nu$  represents  $\nu_e$ ,  $\bar{\nu}_e$ ,  $\nu_\mu$ ,  $\bar{\nu}_\mu$ ,  $\nu_\tau$  and  $\bar{\nu}_\tau$ . The EPA and BS subscript on the incoming photon indicates whether the photon is generated from the equivalent photon approximation or beamstrahlung.

to the impact point (IP). Any hits that have are measured outside of these windows are not used in the reconstruction.

## 2.3 Modelling of Anomalous Gauge Couplings

The samples that were sensitive to the anomalous gauge couplings  $\alpha_4$  and  $\alpha_5$  were generated using Whizard version 1.97, instead of the previously quoted version 1.95. This change was required as version 1.97 contained a unitarisation scheme that ensured

cross-sections for processes involving longitudinal gauge boson scattering did not violate unitarity at the energies considered here.

Two alternative methods exist for modelling the sensitivity of the vector boson scattering process to the anomalous gauge couplings  $\alpha_4$  and  $\alpha_5$ . The first is to generate multiple samples with different values of  $\alpha_4$  and  $\alpha_5$  and the second is to generate a single sample with  $\alpha_4 = 0$  and  $\alpha_5 = 0$  and reweight that sample. The latter approach was taken in this analysis as the former approach is impractical when considering a fine sampling of the  $\alpha_4$  and  $\alpha_5$  space.

Event weights,  $w$ , are calculated according to the ratio of the matrix elements,  $M$ , for the particular event configuration [31]

$$w(\alpha_4, \alpha_5) = \frac{|M(event, \alpha_4, \alpha_5)|^2}{|M(event, 0, 0)|^2}. \quad (2.2)$$

Figure 2.4 shows the dependence of the event weights on  $\alpha_4$  and  $\alpha_5$  for four individual  $\nu\nu qqqq$  final state events, generated for  $\sqrt{s} = 1.4$  TeV.

Only final states involving contributions from massive gauge boson quartic vertices require reweighting. Whizard was used to evaluate the cross-sections for all final states shown in table 2.1 with  $\alpha_4 = \alpha_5 = 0$  and with  $\alpha_4 = \alpha_5 = 0.05$ . Only the three final states shown in table 2.2 were found to have a dependency on  $\alpha_4$  and  $\alpha_5$ .

Final State	Cross Section [fb] ( $\alpha_4 = \alpha_5 = 0.00$ )	Cross Section [fb] ( $\alpha_4 = \alpha_5 = 0.05$ )	Percentage Change[%]
$e^+e^- \rightarrow \nu\nu qqqq$	24.7	34.6	+40.1
$e^+e^- \rightarrow \nu l qqqq$	115.3	113.0	-2.0
$e^+e^- \rightarrow ll qqqq$	62.1	68.6	+10.5

**Table 2.2:** Cross sections for selected processes showing the effect of the anomalous gauge couplings  $\alpha_4$  and  $\alpha_5$  for  $\sqrt{s} = 1.4$  TeV.

To maximise the sensitivity to the anomalous gauge couplings, the  $\nu\nu qqqq$  final state is used to define signal in this analysis. The  $l\nu qqqq$  and  $ll qqqq$  final states are treated as backgrounds that are invariant to changes in  $\alpha_4$  and  $\alpha_5$  because they have a much reduced sensitivity to the anomalous gauge couplings in comparison to the  $\nu\nu qqqq$  final state. Furthermore, the  $l\nu qqqq$  and  $ll qqqq$  final states can be easily vetoed during event selection because of the presence of the primary lepton, which means the sensitivity of

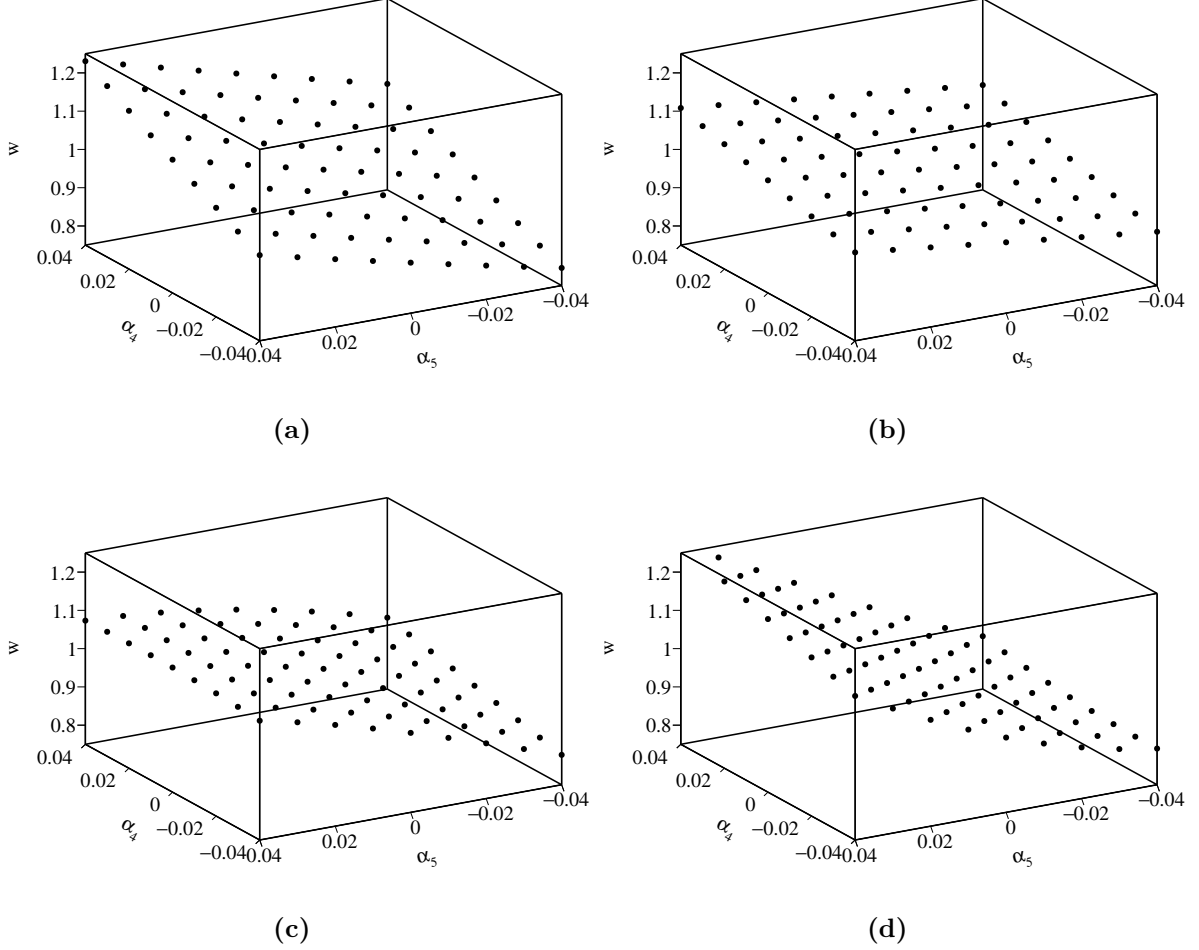


**Figure 2.4:** The event weights,  $w$ , determined by the generator as a function of the anomalous couplings  $\alpha_4$  and  $\alpha_5$  for a selection of  $\nu\nu qqqq$  final state events for  $\sqrt{s} = 1.4$  TeV.

these states to the anomalous gauge couplings will have a negligible effect on the results from this study.

Use of the unitarisation scheme in Whizard 1.97, which is needed to ensure cross-sections do not violate unitarity when studying anomalous gauge couplings at CLIC like energies, requires a unit CKM matrix [31]. The impact of this requirement was examined by comparing several reconstructed and MC distributions for  $\nu\nu qqqq$  final state events generated with Whizard using a Standard Model and unit CKM matrix. No significant differences were observed, which indicates that enforcing a unit CKM matrix when generating the  $\nu\nu qqqq$  final state samples did not significantly affect this analysis.

## 2.4 Data Analysis

The following section contains a description of how the variables used throughout the anomalous gauge coupling sensitivity study are determined.

### 2.4.1 Limiting Beam Related Backgrounds

During the reconstruction, after the inner detector tracks have been reconstructed, the CLICTrackSelection processor is applied, which vetoes poorly reconstructed and fake tracks by applying simple quality cuts to the number of hits in the tracking sub-detectors. The CLICTrackSelection processors also reject tracks where the time of arrival at the calorimeter differs by more than 50 ns between a straight line of flight and a helix fit to the track. Applying this cut ensures that associations made between charged particles tracks and calorimetric energy deposits are consistent.

Following the reconstruction, the CLICPfoSelector processor is applied to remove reconstructed particle flow objects (PFOs) that originate from beam related backgrounds. This processor applies cuts on the  $p_T$  and timing information of the PFOs, which vary as a function of position in the detector and the PFO type to target regions of the detector where backgrounds are more prominent, e.g. low  $p_T$  for  $\gamma\gamma \rightarrow \text{hadrons}$  events. Three configurations of the CLICPfoSelector have been developed for the CLIC environment and were considered in this analysis. They are, in order of increasing background rejection, the Loose, Default and Tight selections [29].

### 2.4.2 Jet Finding

After the application of the CLICPfoSelector, the MarlinFastJet processor, a wrapper for the FastJet [32] processor, was used to cluster each event into four jets. These jets are then paired up to form two candidate bosons working under the assumption that the correct pairing is achieved when the difference between the invariant masses of the candidate bosons is a minima. In the case of the signal final state,  $\nu\nu qqqq$ , it is assumed that the four jets and two candidate bosons map onto the four primary quarks and two outgoing bosons in the vector boson scattering process. The jet clustering was performed using the longitudinally invariant  $k_t$  jet algorithm in exclusive mode. The longitudinally invariant  $k_t$  algorithm proceeds as follows

1. Determine the  $k_t$  distance,  $d_{ij}$ , for each pair of particles,  $i$  and  $j$ , and the beam,  $d_{iB}$ , distance for each particle,  $i$ . These distances are defined as

$$d_{ij} = \min(p_{ti}^2, p_{tj}^2) \Delta R_{ij}^2 / R^2 , \quad (2.3)$$

$$d_{iB} = p_{ti}^2 , \quad (2.4)$$

where  $\Delta R_{ij}^2 = (y_i - y_j)^2 + (\phi_i - \phi_j)^2$ ,  $p_{ti}$  is the transverse momentum of particle  $i$ ,  $y_i$  is the rapidity of particle  $i$ ,  $\phi_i$  is the azimuthal angle of the direction of travel of particle  $i$  and  $R$  is a configurable parameter that typically is of the order of 1.

2. Find the minimum distance,  $d_{\min}$ , of all the  $k_t$  and beam distances. If the minimum occurs for a  $k_t$  distance, particles  $i$  and  $j$  are merged, summing their 4-momenta. If the beam distance is the minima, particle  $i$  was declared to be part of the "beam" jet and the particle is removed from the list of particles and not included in the final jet output.
3. Repeat until the desired number of jets is created. Alternatively, in inclusive mode this would be repeated until no particles are left in the event.

Two other clustering algorithms were considered, however, they were found to be inappropriate for the experimental conditions at CLIC. These alternative algorithm choices are applied in the same manner as the longitudinally invariant  $k_t$  algorithm, however, they differ in the definition of  $d_{ij}$  and  $d_{iB}$ . Figure 2.5 shows the distribution of the invariant mass of the candidate bosons for  $\sqrt{s} = 1.4$  TeV  $\nu\nu qqqq$  final state events for each of the jet algorithms considered. The candidate boson masses are determined by forcing the events into 4 jets and then pairing the jet pairs to form candidate bosons. The jet pairing configuration is determined by pairing jets such that the mass differences between the two candidate bosons is a minimum.

The first alternative jet algorithm considered was the  $k_t$  algorithm for  $e^+e^-$  colliders, the  $e^+e^-k_t$  or Durham algorithm. In this algorithm  $d_{iB}$  is not used and

$$d_{ij} = 2\min(E_i^2, E_j^2)(1 - \cos\theta_{ij}) , \quad (2.5)$$

where  $\theta_{ij}$  is the opening angle of particles  $i$  and  $j$  and  $E_i$  is the energy of particle  $i$ . In the collinear limit  $d_{ij}$  corresponds to the relative transverse momenta of the particles. The major failure of this algorithm when applied to CLIC is the absence of  $d_{iB}$ , which leads to large numbers of beam related background particles being associated to jets. As figure 2.5 shows, the invariant mass of the paired jets, which should peak around

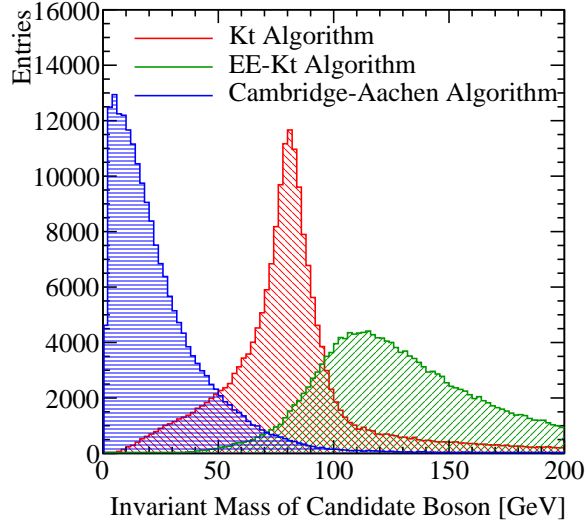


**Figure 2.5:** The reconstructed masses for different choices of jet algorithm for  $\sqrt{s} = 1.4$  TeV  $\nu\nu qqqq$  final state events. These samples should be dominated by vector boson scattering involving pairs of outgoing W bosons and so it is expected that a peak at the W boson mass,  $m_W = 80.385 \pm 0.015$  GeV [3], should be observed. In the case of the  $k_t$  algorithm and the  $e^+e^-k_t$  algorithm an R parameter of 0.7 was used. All distributions show raw number of events.

the W and Z boson masses, is much larger than expected, due to the presence of these backgrounds. Also this algorithm is not invariant to boosts along the beam direction meaning that it is inappropriate for use at CLIC given the beam induced backgrounds modify the nominal collision kinematics.

The second alternative jet algorithm considered was the Cambridge-Aachen jet algorithm where

$$d_{ij} = \Delta R_{ij}^2 / R^2, \quad (2.6)$$

$$d_{iB} = 1. \quad (2.7)$$

This algorithm performs poorly as it does not account for the transverse momentum or the energy of the particles being clustered. In essence, this is a cone clustering algorithm with a cone radius defined through  $\Delta R_{ij} = R$ , which even for large R was found to discard too much energy in the event to be useful for this analysis. This can be seen in figure 2.5 where the invariant mass of the paired jets is much lower than expected. This algorithm is appropriate for events that contain highly boosted jets, however, at CLIC the jets are too disperse for this algorithm to be successful.

### 2.4.2.1 Optimal Jet Finding Algorithm

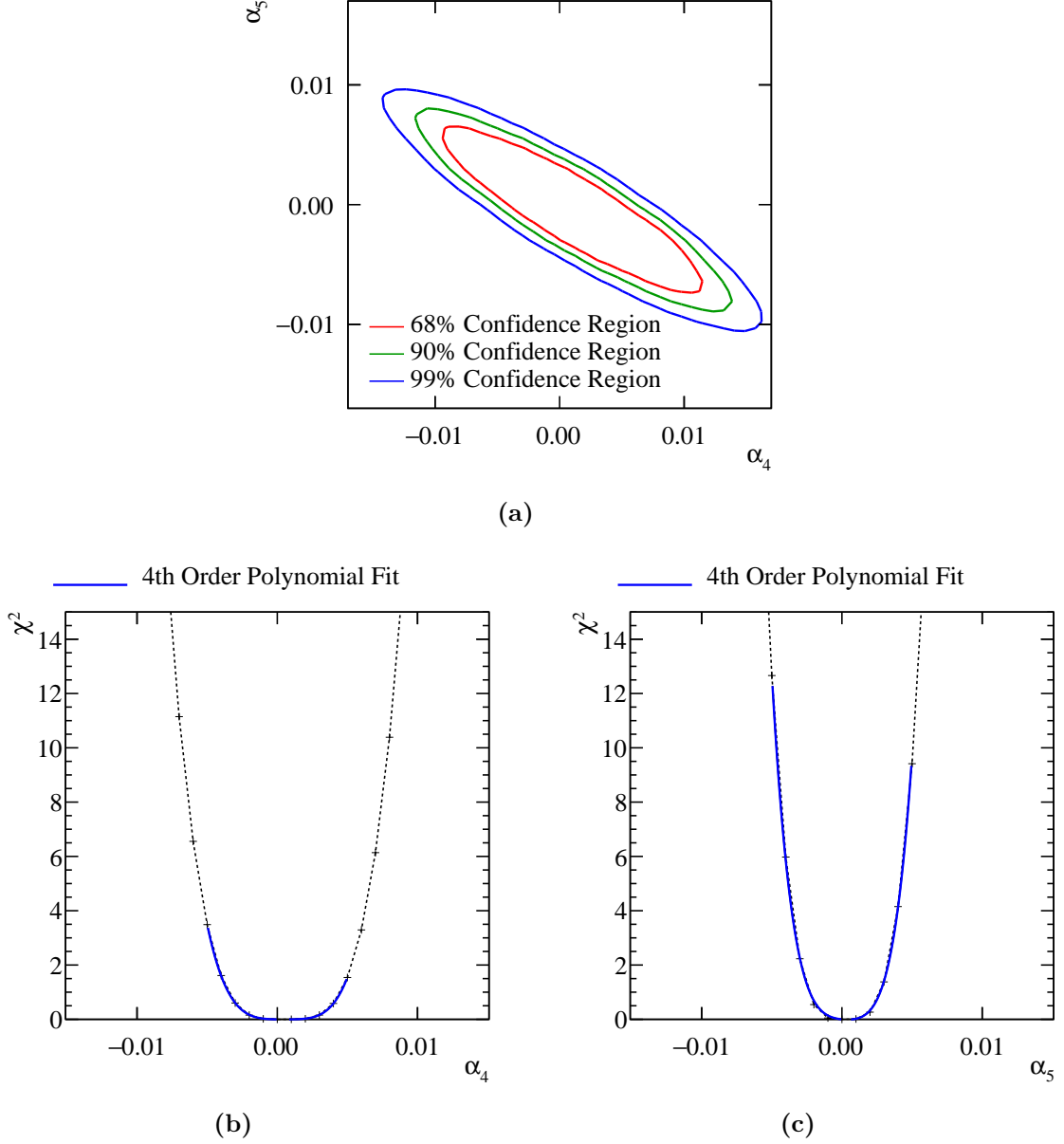
Optimisation of the jet finding procedure was performed on both the PFO selection and the value of the R parameter used in the longitudinally invariant  $k_t$  algorithm. The optimisation procedure involved performing the sensitivity study, described in section 2.6, using solely the  $\nu\nu qqqq$  signal final state. This methodology ensures that the optimisation was done with respect to the physics of interest without having to perform the jet reconstruction for the large number of background events for each jet algorithm configuration considered.

Table 2.3 shows the one  $\sigma$  confidence limits on the measurement of  $\alpha_4$  and  $\alpha_5$  obtained using the  $\nu\nu qqqq$  signal final state only at  $\sqrt{s} = 1.4$  TeV for different jet algorithm configurations. These confidence limits represent the idealised sensitivity of the CLIC experiment to the anomalous gauge couplings. Once the effects of backgrounds and event selection are included in the analysis, these confidence limits will increase in size.

R Parameter	PFO Selection		
	Tight Selected PFOs	Selected PFOs	Loose Selected PFOs
0.7	$-0.0039 < \alpha_4 < 0.0051$	$-0.0035 < \alpha_4 < 0.0047$	$-0.0037 < \alpha_4 < 0.0047$
	$-0.0027 < \alpha_5 < 0.0031$	$-0.0025 < \alpha_5 < 0.0031$	$-0.0024 < \alpha_5 < 0.0028$
0.9	$-0.0036 < \alpha_4 < 0.0047$	$-0.0035 < \alpha_4 < 0.0045$	$-0.0035 < \alpha_4 < 0.0045$
	$-0.0026 < \alpha_5 < 0.0031$	$-0.0023 < \alpha_5 < 0.0027$	$-0.0022 < \alpha_5 < 0.0027$
1.1	$-0.0036 < \alpha_4 < 0.0047$	$-0.0036 < \alpha_4 < 0.0048$	$-0.0036 < \alpha_4 < 0.0046$
	$-0.0026 < \alpha_5 < 0.0031$	$-0.0025 < \alpha_5 < 0.0029$	$-0.0024 < \alpha_5 < 0.0028$

**Table 2.3:** One  $\sigma$  confidence limits on the measurement of  $\alpha_4$  and  $\alpha_5$  obtained using the  $\nu\nu qqqq$  signal final state only at  $\sqrt{s} = 1.4$  TeV for different jet algorithm configurations.

The configuration for the jet algorithm for the  $\sqrt{s} = 1.4$  TeV analysis was chosen as selected PFOs with an R parameter of 0.9. While the loose PFO selection gives a marginally better performance, the selected PFO selection was preferred to minimise the effects of the  $\gamma\gamma \rightarrow \text{hadrons}$  background. Figure 2.6a shows confidence contours, given a null hypothesis of  $\alpha_4 = \alpha_5 = 0$ , for the selected PFO and R parameter of 0.9 jet algorithm configuration for  $\sqrt{s} = 1.4$  TeV. Figures 2.6b and 2.6c show the one dimensional  $\chi^2$  distribution for  $\alpha_4$  and  $\alpha_5$ , assuming  $\alpha_5 = 0$  and  $\alpha_4 = 0$  respectively, for the same configuration.



**Figure 2.6:**  $\chi^2$  sensitivity distributions from a fit to  $M_{VV}$  for the signal  $qqqq\nu\nu$  final state only for  $\sqrt{s} = 1.4$  TeV. These results use the optimal jet algorithm configuration of selected PFOs and an R parameter of 0.9 in the  $k_t$  algorithm. (a)  $\chi^2$  sensitivity contours in  $\alpha_4$  and  $\alpha_5$  space. (b)  $\chi^2$  as a function of  $\alpha_4$  assuming  $\alpha_5 = 0$ . (c)  $\chi^2$  as a function of  $\alpha_5$  assuming  $\alpha_4 = 0$ . All distributions are normalised to an integrated luminosity of  $\mathcal{L}_{int} = 1.5 \text{ ab}^{-1}$ .



### 2.4.3 Lepton Finding

An isolated lepton finder was included in the analysis chain to reject background final states containing primary leptons. Leptons produced via hadronisation are unlikely to be flagged as isolated because all hadronisation products are boosted along the direction of the parent quark. This means isolated leptons are likely to correspond to primary leptons, which makes the number of isolated leptons a powerful discriminating variable to use in event selection.

The isolated lepton finder determines whether a PFO is an electron or muon by first checking that the PFO has a single charged particle track associated to it. If that is the case, the calorimetric energy deposits of the PFO are examined to see if they are consistent with what is expected for an electron or muon. If they are consistent with expectations, the properties of the charged particle track are examined to determine whether the track originates from the IP. If the PFO is deemed to have originated from the IP, isolation checks, which examine the energy deposited in the calorimeters within a cone surrounding the PFO, are applied to determine whether the particles belongs to a jet. If the PFO does not appear to belong to a jet then it is counted as an isolated lepton. The fraction of events rejected by the lepton finder is summarised in table 2.4.

Final State	$\epsilon_{\text{Lepton Finding}}$
$e^+e^- \rightarrow \nu\nu qqqq$	99.7
$e^+e^- \rightarrow \nu lqqqq$	48.9

**Table 2.4:** The fraction of events rejected by of isolated lepton finding for  $\sqrt{s} = 1.4$  TeV for the  $\nu\nu qqqq$  and  $\nu lqqqq$  final states.

### 2.4.4 Discriminant Variables

The next stage of the analysis involved the calculation of a number of event-based variables that were found to be useful for this analysis. The variables that were calculated are as follows

- **Particle level** variables:
  - Number of PFOs in each jet;
  - Energy of the highest energy PFO;

- Energy of the highest energy electron;
- Cosine of the polar angle of the highest energy track;
- The number of isolated leptons found using the isolated lepton finder.

• **Candidate boson** variables:

- Energy of the candidate bosons;
- Invariant mass of the candidate bosons;
- Acolinearity of the candidate boson pair, which is defined as 180 degrees minus the opening angle of the pair of bosons in the rest frame of the detector.

• **Event based** variables:

- The invariant mass of the visible system,  $M_{VV}$ ;
- The vector sum of the transverse momentum of all PFOs in the event;
- Sphericity, defined through the sphericity tensor  $S^{ab}$ ;

$$S^{ab} = \frac{\sum_i p_i^\alpha p_j^\alpha}{\sum_{i,\alpha=1,2,3} |p_i^\alpha|^2} \quad (2.8)$$

Where  $p_i$  are the components of the momenta of PFO  $i$  in the rest frame of the detector and the sum  $\sum_i$  runs over all particles in the event. Sphericity is defined as  $S = \frac{3}{2}(\lambda_2 + \lambda_3)$ , where  $\lambda_i$  are the eigenvalues of the sphericity tensor defined such  $\lambda_1 \geq \lambda_2 \geq \lambda_3$ . This provides a measure of how spherical the reconstructed event topology is with isotropic events having  $S \approx 1$ , while two jet events have  $S \approx 0$ .

• **Jet clustering parameters** variables:

- The  $y_{ij}$  variables where  $i = 3, 4$  and  $j = i + 1$ . These are the smallest  $k_t$  distance found when combining  $j$  jets into  $i$  jets.

### 2.4.5 Jet Energy Resolution at CLIC

The importance of the jet energy resolution, which is extensively discussed in chapters ?? and ??, should be emphasised at this point. Many of the discriminant variables that are calculated for this analysis are dependant upon the jet energy resolution. In particular,

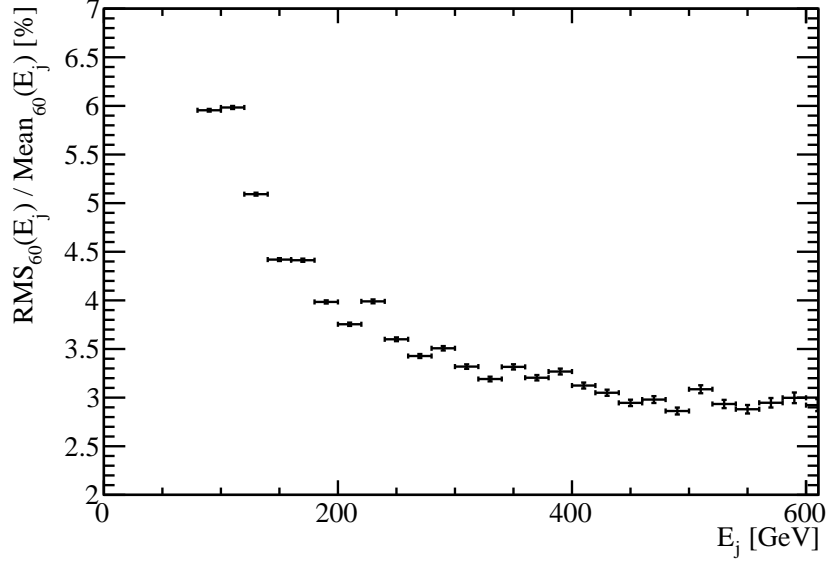


**Figure 2.7:** The jet energy resolution as a function of the jet energy for the  $\nu\nu\text{qqqq}$  final state for  $\sqrt{s} = 1.4$  TeV.

all variables related to the candidate bosons that are formed from pairing up jets, are dependent upon the measurement of jet energies.

Figure 2.7 shows the jet energy resolution as a function of the MC jet energy for the  $\nu\nu\text{qqqq}$  event sample used in the  $\sqrt{s} = 1.4$  TeV analysis. The MC jet energy was obtained by pairing up quarks appearing in the final state to the reconstructed jets. The events were then binned in terms of their MC jet energy and the jet energy resolution calculated for each bin. When calculating the jet energy resolution, a narrower range of jet energies was used in compared to previous studies, 60% of the data with narrowest RMS as opposed to 90%, to minimise the effects of jet finding and beam-induced backgrounds. The jet energy resolutions reported here are worse than those quoted in earlier chapters. This is to be expected given the effects of jet finding and beam-induced backgrounds.

## 2.5 Event Selection

This section discusses the event selection procedure. The goal of this procedure is to isolate the  $\nu\nu\text{qqqq}$  final state from the background final states, i.e. those containing two and four primary quarks. The procedure consists of a set of preselection cuts followed by the application of a multivariate analysis (MVA). All event numbers have

been normalised, prior to event selection, to an integrated luminosity of  $\mathcal{L}_{int} = 1.5 \text{ ab}^{-1}$  for the  $\sqrt{s} = 1.4 \text{ TeV}$  analysis and  $\mathcal{L}_{int} = 2 \text{ ab}^{-1}$  for the  $\sqrt{s} = 3 \text{ TeV}$  analysis.

### 2.5.1 Preselection

A refined selection of the  $\nu\nu qqqq$  signal final state is achieved using a MVA, however, to ensure efficiency in the training and application of that MVA a number of simple preselection cuts were developed to veto obvious background final states prior to the application of the MVA. Preselection cuts were applied to the transverse momentum of the system and the number of isolated leptons found in the event. The raw distributions of these variables is shown in figure 2.8 and based on these distributions the following cuts were applied

- Transverse momentum of system  $> 100 \text{ GeV}$ . This cut is effective due to the presence of missing energy in the form of neutrinos in the signal final state.
- Number of isolated leptons in system  $= 0$ . This cut is effective as the signal final state does not contain leptons, while numerous background final states do.

The impact of these preselection cuts can be found in table 2.5, which can be found on page 38.

### 2.5.2 Multivariate analysis

Having established the preselection cuts, a MVA was applied using the TMVA toolkit [33], to refine the event selection. The signal and background final state samples were separated into two equally sized samples; one sample was used to independently train the MVA and the other sample was used in the subsequent analysis.

The performance of several MVA classifiers was examined to determine the optimal classifier for this analysis. The MVA classifiers considered were [33]:

- **Boosted Decision Tree (BDT)**. Decision trees are formed by the sequential application of cuts that split the data into multiple classes. After the application of the final cut, the remaining classes are used to classify whether the input event corresponds to signal or background. Boosting a decision tree involves the use of several decision trees. A single classifier output is obtained from a weighted average

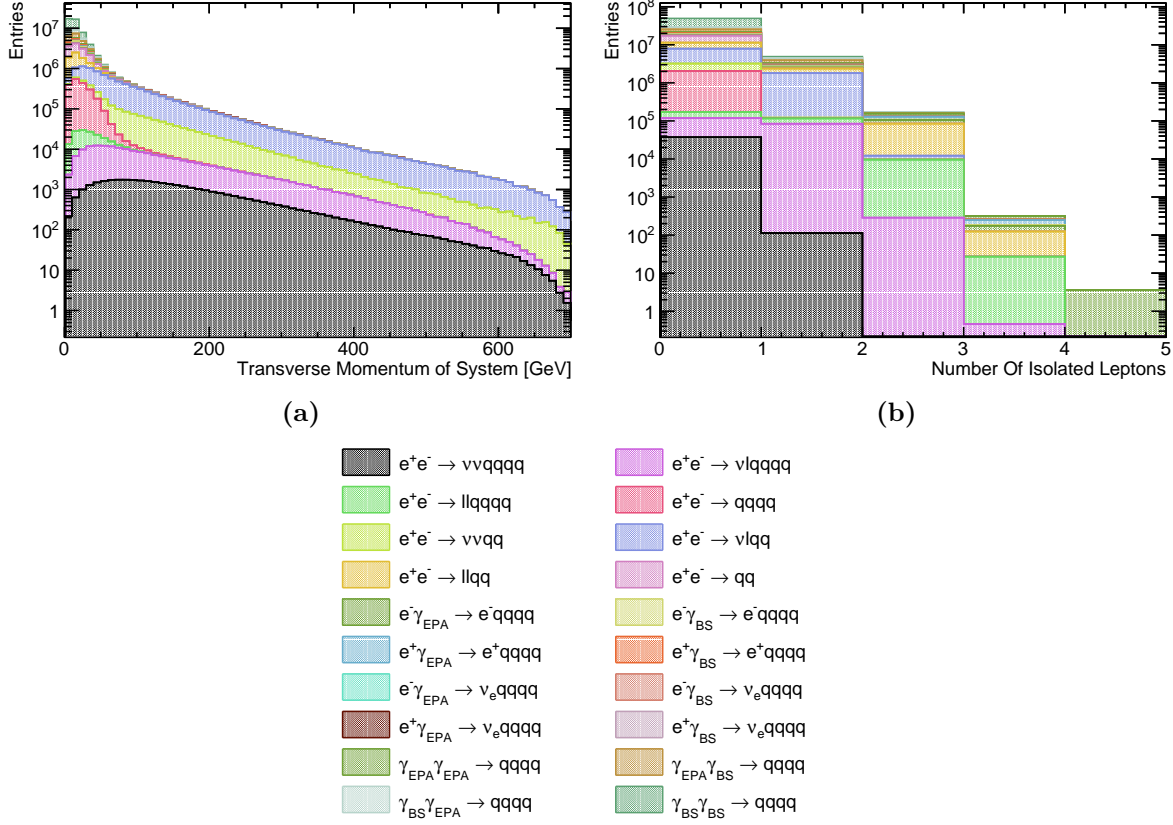


**Figure 2.8:** Distribution of the preselection cut variables for  $\sqrt{s} = 1.4$  TeV: (a) the transverse momentum of the visible system; and (b) the number of isolated leptons in the system. All distributions are normalised to an integrated luminosity of  $\mathcal{L}_{int} = 1.5 \text{ ab}^{-1}$ .

of the individual decision trees. The cuts applied in the decision tree are determined using the training sample.

- **$k$ -Nearest Neighbour (KNN).** For a given input event, the  $k$  closest neighbours from the training sample are found. The classifier for that input event is determined as the fraction of those  $k$  events that belong to the signal sample. Distances in this classifier are defined as the Euclidean distance between events in the  $n$ -dimensional space of the variables used for training the classifier. Weights are applied when calculating the distances to account for the differing widths of the input variable distributions. The value of  $k$  used in this analysis was 20.
- **Multilayer Perceptron (MLP).** This is an example of a neural network. Neural networks consist of an interconnected series of neurons each with a different response to a set of input signals. The signal for the first layer of neurons in this case are

the event variables used to train the MVA. The input signal proceeds to travel through several layers of neurons. The number of neurons in a given layer is reduced as the number of layers passed through increases until two neurons are left, one corresponding to signal and the other background. The neuron giving the larger response in the final layer determines the event classifier. The training sample is used to determine the response of each neurons in the network.

- **Fisher and H-Matrix Discriminants.** These procedures involve the calculation of a hyperplane in  $n$ -dimensional space that maximally separates signal and background events in the training sample. The location of an input event in that  $n$ -dimensional space with respect to that hyperplane determines the classifier for the event. The hyperplane is determined by maximising the differences between the means of the input event variables normalised by a measure of their spread. Both the Fisher and H-Matrix discriminants search for the hyperplane in  $n$ -dimensional space, however, the Fisher discriminant begins this procedure by transforming the input variables into a variable space with zero linear correlations.
- **Likelihood.** The likelihood is determined using the probability density function (PDF) for each of the input variables. PDFs are determined using the training sample for both signal and background events. For a given event, the likelihood is given by the product of the probability of obtaining each of the input variables for that event. The signal and background likelihoods are calculated using the signal and background PDFs respectively and the ratio of the signal likelihood to the sum of the signal and background likelihoods gives the event classifier.

The input variables used for these MVA classifiers were:

- Number of PFOs in each jet;
- Energy of the highest energy PFO;
- Energy of the highest energy electron;
- Cosine of the polar angle of the highest energy track;
- Energy of the candidate bosons;
- Invariant mass of the candidate bosons;
- Acolinearity of the candidate boson pair;
- The vector sum of the transverse momentum of all PFOs in the event;

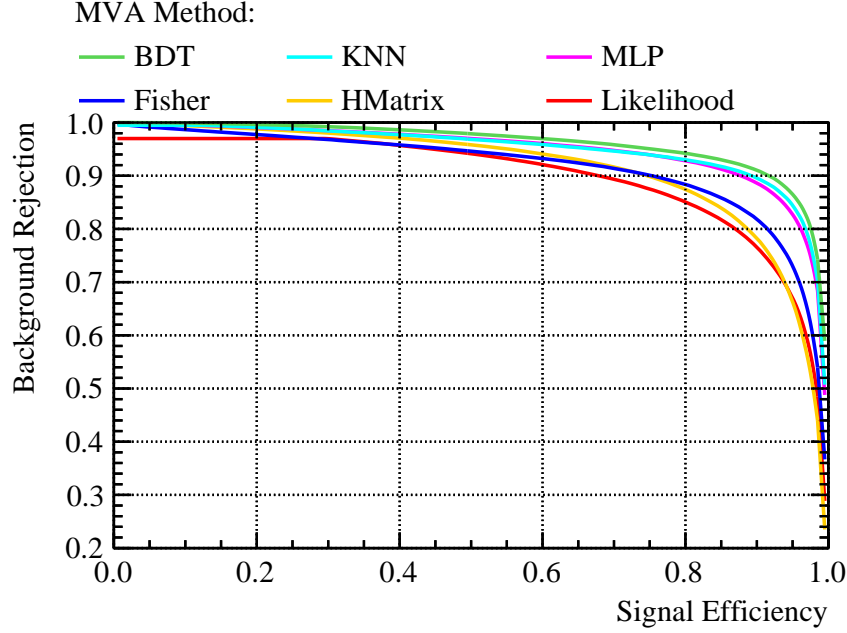


**Figure 2.9:** Background rejection as a function of signal efficiency for a variety of MVA options for  $\sqrt{s} = 1.4$  TeV.

- The sphericity of the event;
- The derived jet clustering parameter variables  $-\log_{10}(y_{ij})$  where  $y_{ij}$  are jet clustering parameters,  $i = 3, 4$  and  $j = i + 1$ .

Figure 2.9 shows the background rejection, which is equivalent to one minus the background efficiency, as a function of signal efficiency for various MVA classifiers. Efficiency is defined as the fraction of events classified as signal by the MVA. The efficiencies reported by TMVA are calculated after the application of the preselection cuts, which are described in section 2.5.1.

The classifier giving the optimal performance in terms of signal efficiency and background rejection was the BDT. The performance of the BDT was optimised further by varying the number of trees used and the depth of the trees. An optimal significance,  $S/\sqrt{(S+B)}$ , where  $S$  and  $B$  are the number of signal and background events passing the preselection respectively, of 52.7 was obtained using the optimised BDT.

### 2.5.3 Event Selection Summary

The event selection is summarised using the distribution of the invariant mass of the candidate bosons, which for the signal final state should peak around the W mass. This distribution is shown in figure 2.10 with: no event selection; with the preselection cuts applied; and with both preselections cuts and MVA applied. The event selection efficiencies are also summarised in table 2.5.

As expected the dominant background processes after the MVA is applied are those that have the same topology as the signal process, i.e. four primary quarks with missing energy. Two smaller sources of background are also present: two jet events with missing energy that are confused with four jet events with missing energy and events where a lepton is not properly reconstructed causing the event to look like four jets and missing energy.

## 2.6 Anomalous Coupling Fitting Methodology

This section describes the procedure used for constructing the  $\chi^2$  surface and the subsequent confidence contours used to determine the sensitivity of CLIC to the anomalous gauge couplings  $\alpha_4$  and  $\alpha_5$ .

### 2.6.1 Sensitive Distribution

The sensitivity of CLIC to the anomalous gauge couplings will be determined through the use of a  $\chi^2$  fit. Three variables showing sensitivity to the anomalous gauge couplings were considered for use in the  $\chi^2$  fit:

- $M_{VV}$ . The invariant mass of the visible system;
- $\cos\theta_{Bosons}^*$ . The angle between the boost direction and the back-to-back candidate bosons in the rest frame of the visible system;
- $\cos\theta_{Jets}^*$ . The angle between the boost direction and the back-to-back jets in the rest frame of the candidate bosons. As each event contains two candidate bosons, there are two  $\cos\theta_{Jets}^*$  variables per event.



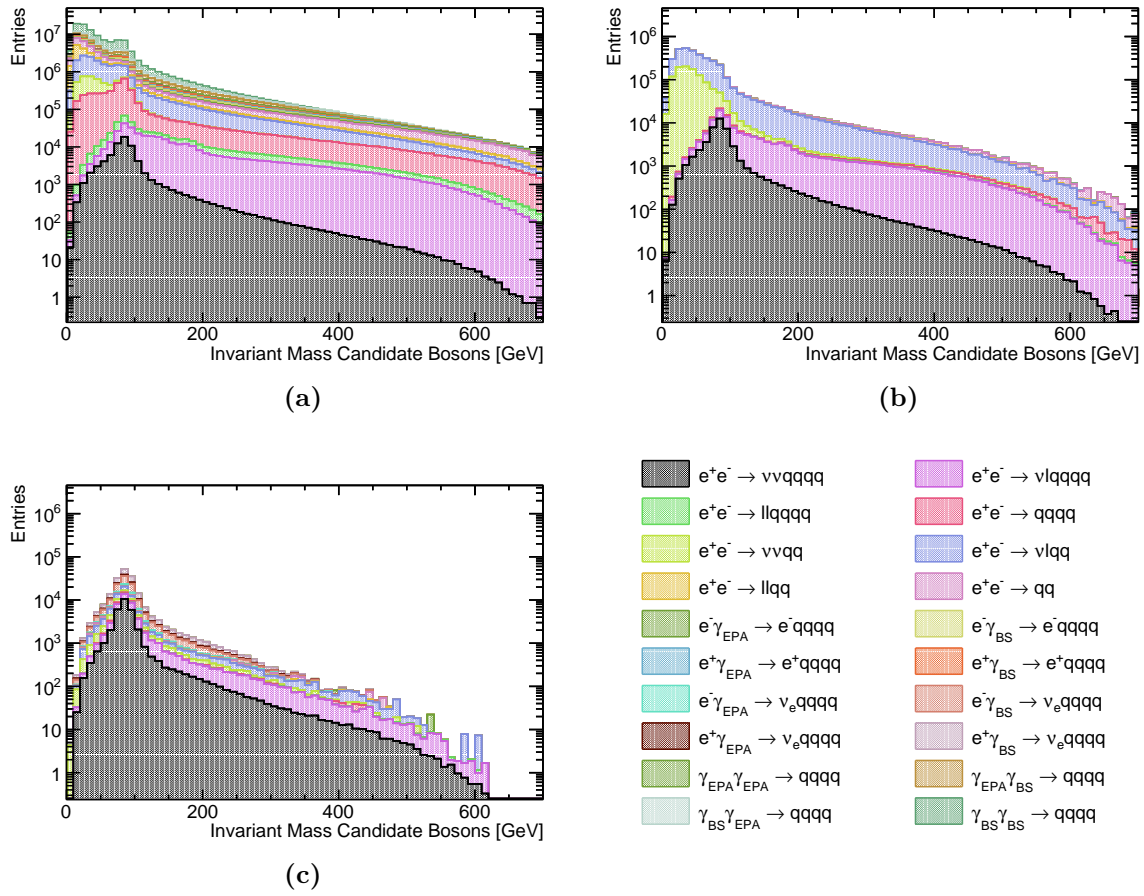


**Figure 2.10:** Impact of preselection and MVA on the reconstructed invariant mass of the candidate bosons for  $\sqrt{s} = 1.4$  TeV: (a) no cuts; (b) after preselection; and (c) after preselection and MVA. All distributions correspond to an integrated luminosity of  $\mathcal{L}_{int} = 1.5 \text{ ab}^{-1}$ .

Final State	$\epsilon_{\text{presel}}$	$\epsilon_{\text{BDT}}$	$N_{\text{BDT}}$
$e^+e^- \rightarrow \nu\nu qqqq$	64.1%	44.5%	16,470
$e^+e^- \rightarrow \nu l qqqq$	26.1%	5.2%	8,582
$e^+e^- \rightarrow ll qqqq$	0.8%	0.1%	100
$e^+e^- \rightarrow qq qq$	0.3%	0.1%	1,698
$e^+e^- \rightarrow \nu\nu qq$	43.4%	0.5%	5,351
$e^+e^- \rightarrow \nu l qq$	19.1%	0.1%	9,319
$e^+e^- \rightarrow ll qq$	0.1%	-	234
$e^+e^- \rightarrow qq$	0.6%	-	1,586
$e^- \gamma_{\text{EPA}} \rightarrow e^- qq qq$	0.2%	-	48
$e^- \gamma_{\text{BS}} \rightarrow e^- qq qq$	0.1%	-	42
$e^+ \gamma_{\text{EPA}} \rightarrow e^+ qq qq$	0.3%	-	19
$e^+ \gamma_{\text{BS}} \rightarrow e^+ qq qq$	-	-	65
$e^- \gamma_{\text{EPA}} \rightarrow \nu_e qq qq$	26.0%	9.0%	4,421
$e^- \gamma_{\text{BS}} \rightarrow \nu_e qq qq$	36.1%	15.0%	23,150
$e^+ \gamma_{\text{EPA}} \rightarrow \bar{\nu}_e qq qq$	25.9%	9.2%	4,495
$e^+ \gamma_{\text{BS}} \rightarrow \bar{\nu}_e qq qq$	36.4%	15.3%	23,410
$\gamma_{\text{EPA}} \gamma_{\text{EPA}} \rightarrow qq qq$	0.2%	-	81
$\gamma_{\text{EPA}} \gamma_{\text{BS}} \rightarrow qq qq$	0.1%	-	55
$\gamma_{\text{BS}} \gamma_{\text{EPA}} \rightarrow qq qq$	-	-	53
$\gamma_{\text{BS}} \gamma_{\text{BS}} \rightarrow qq qq$	-	-	0

**Table 2.5:** Event selection efficiencies for  $\sqrt{s} = 1.4$  TeV. In the above table,  $\epsilon_{\text{presel}}$  denotes the number of events passing the preselection as a fraction of the total number of events, while  $\epsilon_{\text{BDT}}$  denotes the number of events passing both the preselection and the BDT as a fraction of the total number of events. The EPA and BS subscript on the incoming photon indicates whether the photon is generated from the equivalent photon approximation or beamstrahlung. Entries with a dash indicate an efficiency of less than 0.1%. The event numbers correspond to an integrated luminosity of  $\mathcal{L}_{\text{int}} = 1.5 \text{ ab}^{-1}$ .

Figure 2.11 shows the distribution of these variables for the  $\nu\nu qqqq$  final state for selected values of the anomalous gauge couplings  $\alpha_4$  and  $\alpha_5$ . A  $\chi^2$  fit to each of these variables was applied to obtain confidence limits on the sensitivity of CLIC to the anomalous gauge couplings, as described in section 2.6.2. The distributions used for the  $\chi^2$  fit contained signal and background events that passed event selection. Table 2.6 shows the one  $\sigma$  confidence limits on the measurement of  $\alpha_4$  and  $\alpha_5$  obtained using

each of the variables considered. The  $M_{VV}$  distribution shows the greatest sensitive to the anomalous gauge couplings; therefore, it will be used by all subsequent  $\chi^2$  fits when reporting sensitivities. This distribution shows the greatest sensitivity of the variables considered because the couplings primarily affect events with large values of  $M_{VV}$  and there are relatively few of these events.

Sensitive Variable	One $\sigma$ Confidence Limits
$M_{VV}$	$-0.0082 < \alpha_4 < 0.0116$
	$-0.0055 < \alpha_5 < 0.0078$
$\cos\theta_{Bosons}^*$	$-0.0111 < \alpha_4 < 0.0155$
	$-0.0082 < \alpha_5 < 0.0110$
$\cos\theta_{Jets}^*$	$-0.0100 < \alpha_4 < 0.0142$
	$-0.0070 < \alpha_5 < 0.0098$

**Table 2.6:** One  $\sigma$  confidence limits on the measurement of  $\alpha_4$  and  $\alpha_5$  obtained at  $\sqrt{s} = 1.4$  TeV. These sensitivities include the affect from backgrounds and event selection.

### 2.6.2 $\chi^2$ Surface and Confidence Limit Definition

A  $\chi^2$  surface was used to determine confidence limits on the anomalous gauge couplings given the null hypothesis that  $\alpha_4 = \alpha_5 = 0$ . This surface is defined as

$$\chi^2 = \sum_i \frac{(O_i - E_i)^2}{E_i}, \quad (2.9)$$

where  $O_i$  is the observed,  $\alpha_4 = \alpha_5 = 0$ , and  $E_i$  the expected,  $\alpha_4 \neq 0$  and  $\alpha_5 \neq 0$ , bin content for bin  $i$  in the distribution of interest. The summation  $\Sigma_i$  runs over bins in the distribution of interest.

When applying the  $\chi^2$  fit to the  $M_{VV}$  distribution, the distribution was binned using 13 bins as shown in figure 2.12. The first bin spanned the invariant mass range between 0 GeV and 200 GeV, this was followed by 11 bins of width 100 GeV ranging from 200 GeV to 1300 GeV and finally the last bin contained all invariant masses above 1300 GeV. The expanded bin widths at the tails of the distribution were chosen to ensure the bin contents were sufficiently large to give a reliable estimate the likelihood function using the  $\chi^2$  parameter. This choice of bin width also ensured the bin contents were sufficiently large to minimise fluctuations arising from individual events with large weights. When applying

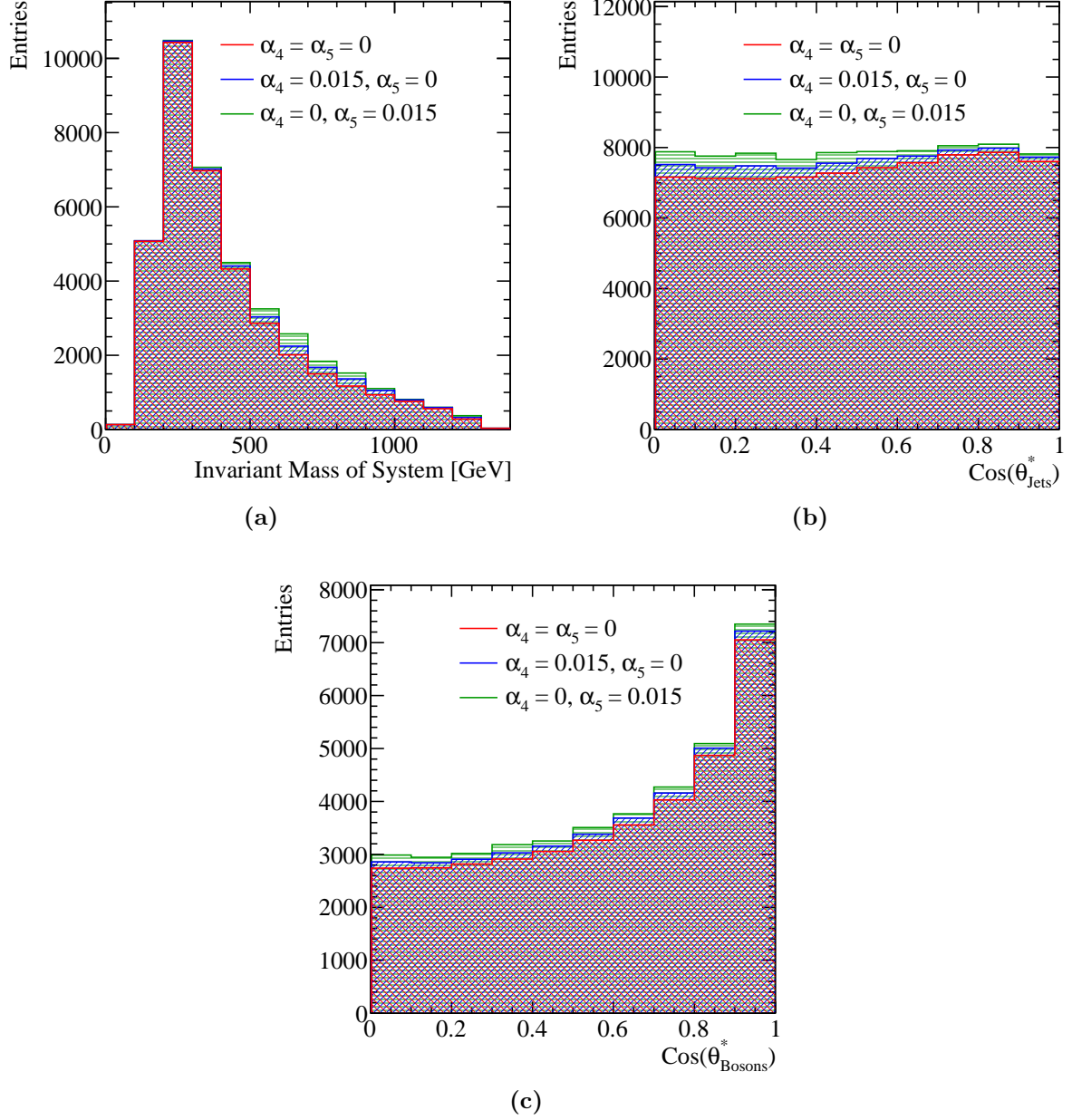


**Figure 2.11:** The distributions of (a)  $M_{VV}$ , (b)  $\cos\theta_{Jets}^*$  and (c)  $\cos\theta_{Bosons}^*$  for selected values of the anomalous gauge couplings  $\alpha_4$  and  $\alpha_5$  for the  $\nu\nu qqqq$  final state for  $\sqrt{s} = 1.4 \text{ TeV}$ . The jet algorithm used was the longitudinally invariant  $k_t$  algorithm with an R parameter of 0.9 and Selected PFOs. All distributions are normalised to an integrated luminosity of  $\mathcal{L}_{int} = 1.5 \text{ ab}^{-1}$ .

the  $\chi^2$  fit to distributions of the  $\cos\theta_{Bosons}^*$  and  $\cos\theta_{Jets}^*$  variables, the distributions were binned using 10 bins ranging from zero to one. As there are two  $\cos\theta_{Jets}^*$  variables per event, the  $\chi^2$  fit was applied to a two dimensional distribution of  $\cos\theta_{Jets}^*$ , where

a distinction between the two  $\cos\theta_{J_{ets}}^*$  variables was made based on the energy of the candidate bosons. The use of a two dimensional distribution in the  $\chi^2$  fit was needed to account for any correlation between the two  $\cos\theta_{J_{ets}}^*$  variables.

Confidence limits describing the sensitivity of the CLIC experiment to the anomalous gauge couplings were found by examining the  $\chi^2$  surface in the space of  $\alpha_4$  and  $\alpha_5$ . Deviations from the minima of this surface, which by construction occurs at  $\alpha_4 = \alpha_5 = 0$ , yield confidence limits that indicate the probability of observing a particular value of  $\alpha_4$  and  $\alpha_5$  given the null hypothesis that  $\alpha_4 = \alpha_5 = 0$ . The confidence limits reported in subsequent sections, 68%, 90% and 99%, are defined using fixed deviations from the minima of  $\chi^2$  surface ( $\Delta\chi^2$ ) of 2.28, 4.61 and 9.21 respectively.

Confidence limits on the individual parameters  $\alpha_4$  and  $\alpha_5$  were determined by setting the corresponding coupling term to zero and examining the remaining one dimensional  $\chi^2$  distribution. A fourth order polynomial was fitted to the minima of this distribution and the one sigma confidence limit defined using  $\Delta\chi^2 = 1$ . The definition of a one sigma confidence limit accounts for changes in the number of degrees of freedom in the fit, therefore, it changes when fixing the corresponding coupling term to zero.

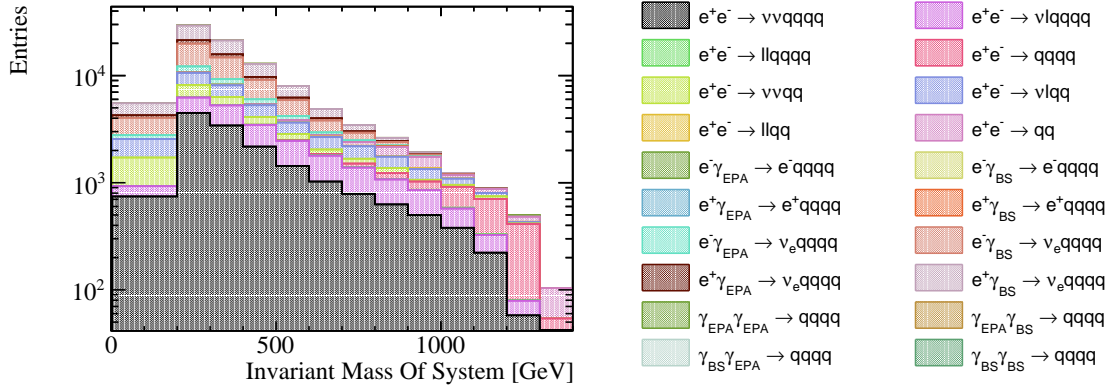


**Figure 2.12:** The distribution of the invariant mass of the system for both signal and background final states that is used in the  $\chi^2$  fit for  $\sqrt{s} = 1.4$  TeV. The distribution includes effect of event selection and corresponds to an integrated luminosity of  $\mathcal{L}_{int} = 1.5 \text{ ab}^{-1}$ .

### 2.6.3 Event Weight Interpolation Scheme

In order to obtain a smooth  $\chi^2$  surface a fine sampling of the event weights in the  $\alpha_4$  and  $\alpha_5$  space is required, however, it is unfeasible to generate a finely sampled grid of event

weights on an event by event basis because event generation is highly CPU intensive. To resolve this issue, an interpolation scheme was applied to determine the event weights within a sampled region of the  $\alpha_4$  and  $\alpha_5$  space. This allows for an infinite sampling of the event weights in the space of  $\alpha_4$  and  $\alpha_5$  without having to call the generator an infinite number of times.

A bicubic interpolation scheme, cubic interpolation along the two dimensions, was applied to the event weights produced by the generator. This procedure is best illustrated by figure 2.13, which shows the interpolated event weight surface superimposed with the raw event weights from the generator for four  $\nu\nu qqqq$  events for  $\sqrt{s} = 1.4$  TeV. This interpolation scheme produces a smooth and continuous surface that can be used for generating a smooth  $\chi^2$  surface.

## 2.7 Results

The sensitivity of the CLIC experiment to the anomalous gauge couplings  $\alpha_4$  and  $\alpha_5$  for  $\sqrt{s} = 1.4$  TeV is shown in figure 2.14a. This result shows the sensitivity after the application of preselection and MVA purposed to remove the included background channels. These contours yield the one  $\sigma$  confidence limits for CLIC operating for  $\sqrt{s} = 1.4$  TeV of

$$-0.0082 < \alpha_4 < 0.0116, \tag{2.10}$$

$$-0.0055 < \alpha_5 < 0.0078. \tag{2.11}$$

### 2.7.1 Systematic Uncertainties

A source of systematic error in this experiment is the uncertainty on the cross-sections for the signal and background processes. Based on the event selection summary shown in table 2.5, the dominant source of background in this analysis comes from the  $e^\pm \gamma_{BS} \rightarrow \nu_e qqqq$  processes. Therefore, uncertainties on the cross-section for these processes, as well as the signal process  $e^+e^- \rightarrow \nu\nu qqqq$ , will be considered.

The uncertainty on the cross-section for a given process is included in the  $\chi^2$  definition through the use of a nuisance parameter. This procedure allows the cross-section for a process to fluctuate, however, the magnitude of the fluctuation,  $r$ , is moderated by an

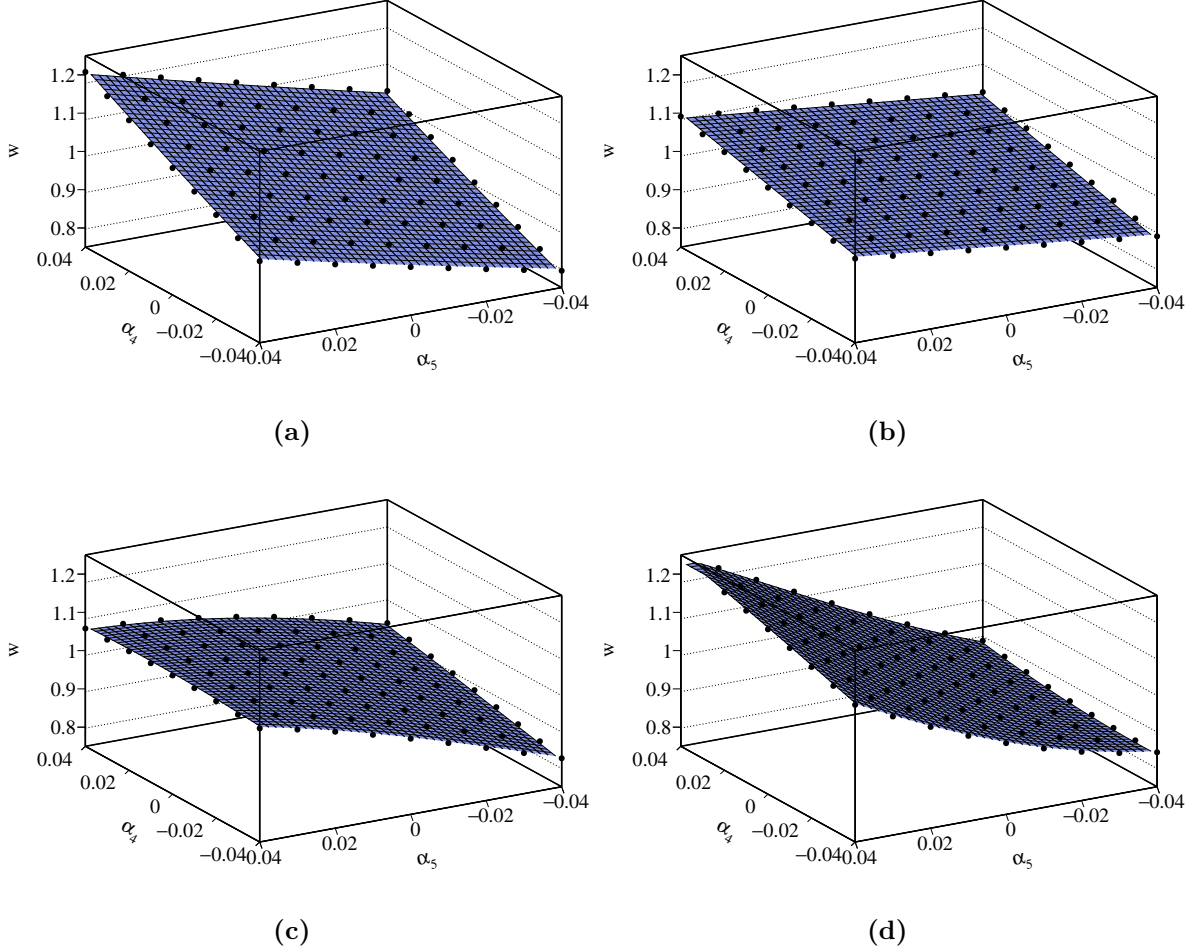


**Figure 2.13:** The event weight,  $w$ , as a function of the anomalous couplings  $\alpha_4$  and  $\alpha_5$  for a selection of  $\sqrt{s} = 1.4$  TeV  $\nu\nu qqqq$  final state events. The black circles show the event weight produced from the generator and the blue surface is determined using bicubic interpolation between these points.

additional penalty term in the  $\chi^2$  as follows

$$\chi^2(r) = \sum_i \frac{(O_i - E_i(r))^2}{E_i(r)} + \frac{(r - 1)^2}{\sigma_r^2}, \quad (2.12)$$

where  $O_i$  is the observed,  $\alpha_4 = \alpha_5 = 0$ , bin content for bin  $i$  in the distribution of  $M_{VV}$  with no background fluctuations and  $E_i(r)$  is the expected,  $\alpha_4 \neq 0$  and  $\alpha_5 \neq 0$ , bin content for bin  $i$  in the distribution of  $M_{VV}$  where the cross-section for the process of interest has been fluctuated by the factor  $r$ . The sum  $\sum_i$  runs over the bins in the  $M_{VV}$  distribution. The  $\sigma_r$  variable is the width of the distribution of  $r$ , which indicates

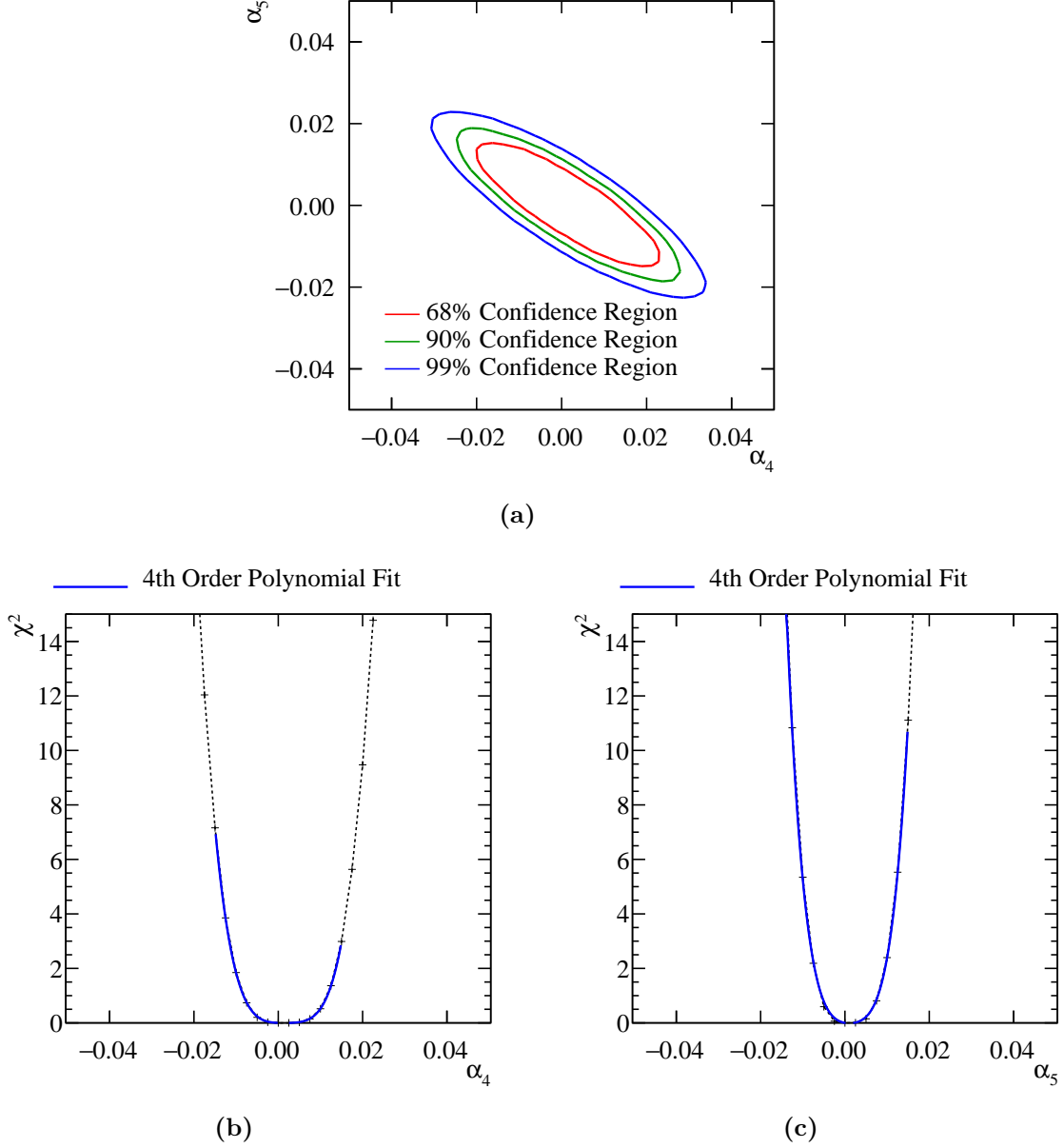


**Figure 2.14:**  $\chi^2$  sensitivity distributions from a fit to  $M_{VV}$  for  $\sqrt{s} = 1.4$  TeV. Results include the effect of backgrounds after the application of a series of preselection cuts and MVA. (a)  $\chi^2$  sensitivity contours in  $\alpha_4$  and  $\alpha_5$  space. (b)  $\chi^2$  as a function of  $\alpha_4$  assuming  $\alpha_5 = 0$ . (c)  $\chi^2$  as a function of  $\alpha_5$  assuming  $\alpha_4 = 0$ .

the uncertainty on the measurement of the cross-section of interest. A  $\chi^2$  surface is constructed in the space of  $\alpha_4$  and  $\alpha_5$  by minimising  $\chi^2(r)$  at each point.

The 68% confidence region is shown with the inclusion of a nuisance parameter for the signal process  $e^+e^- \rightarrow \nu\nu qqqq$  and the dominant background processes  $e^\pm \gamma_{BS} \rightarrow \nu_e qqqq$



in figures 2.15a and 2.15b respectively. Minimal changes in sensitivity are observed when allowing the signal and dominant backgrounds to fluctuate. This can be understood by considering the shape of the  $M_{VV}$  distribution for the signal and dominant background processes, which is shown in figure 2.16. These distribution shows that anomalous couplings primarily affect events with large invariant masses, while both the signal and dominant backgrounds peak at low invariant masses. Therefore, by fluctuating the cross-section for the signal and dominant background processes, it is not possible to gain a significantly better match between the observed and expected bin contents in the  $M_{VV}$  distribution. This is encouraging as despite the  $e^\pm \gamma_{BS} \rightarrow \nu_e qqqq$  backgrounds dominating the  $\chi^2$  fit that determines the sensitivity of CLIC to the anomalous gauge couplings, precise knowledge of their cross-section is not crucial. As the uncertainty on these cross-sections does not significantly affect the confidence regions, no cross-section uncertainties are accounted for when reporting the sensitivity of CLIC to the anomalous gauge couplings elsewhere in this analysis.

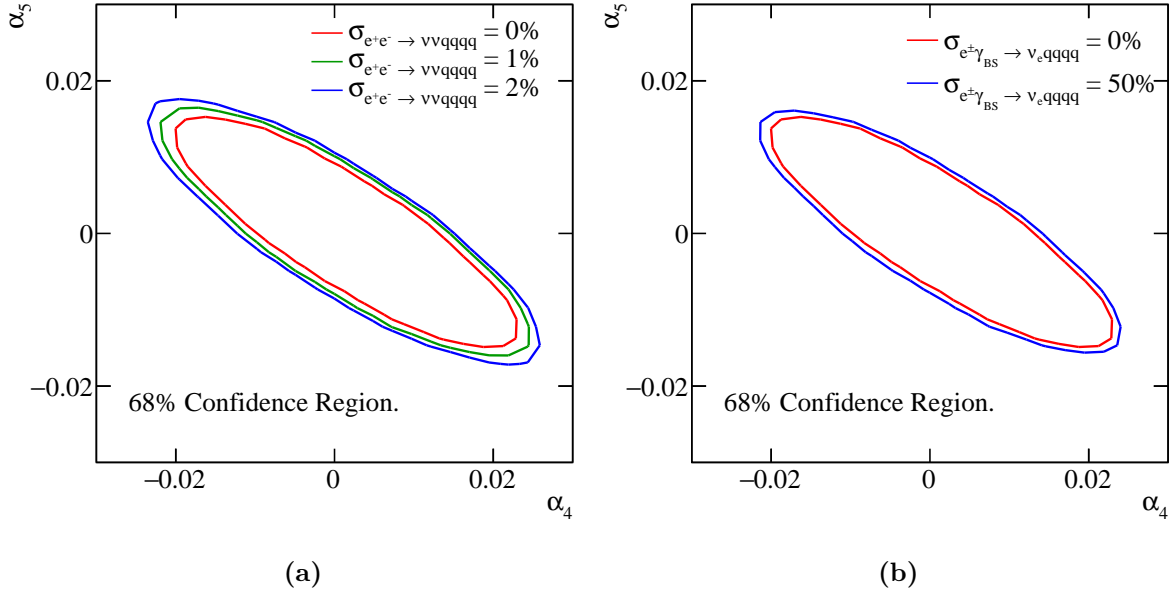


**Figure 2.15:** The 68% confidence region including the effect of uncertainties in the cross-section for (a) the signal process  $e^+e^- \rightarrow \nu\nu qqqq$  and (b) the dominant background processes  $e^\pm \gamma_{BS} \rightarrow \nu_e qqqq$ .

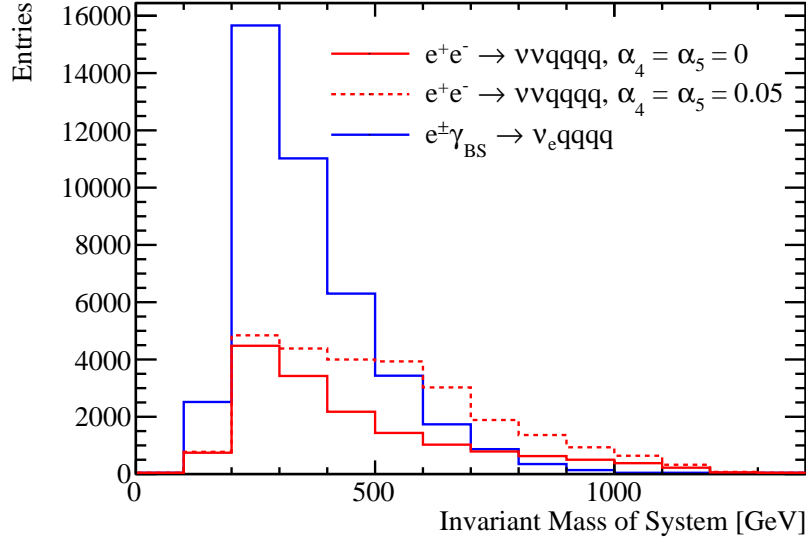


**Figure 2.16:** Distributions of  $M_{VV}$  for the  $e^+e^- \rightarrow \nu\nu qq qq$  signal process, with and without the effect from anomalous couplings, and the combined dominant background processes  $e^\pm \gamma_{BS} \rightarrow \nu_e qq qq$ . All distributions include the effect of event selection and correspond to an integrated luminosity of  $\mathcal{L}_{int} = 1.5 \text{ ab}^{-1}$ .

## 2.8 Sensitivity for $\sqrt{s} = 3 \text{ TeV}$

The anomalous gauge coupling sensitivity study described in this chapter was repeated for CLIC operating for  $\sqrt{s} = 3 \text{ TeV}$ . As this analysis largely mirrors that of the  $\sqrt{s} = 1.4 \text{ TeV}$  analysis, this section focuses on the differences between the two analyses.

The signal and background final states for the  $\sqrt{s} = 3 \text{ TeV}$  analysis were identical to those used for the  $\sqrt{s} = 1.4 \text{ TeV}$  analysis. Cross sections for these processes for  $\sqrt{s} = 3 \text{ TeV}$  are given in table 2.7. The data analysis and event selection procedures used for  $\sqrt{s} = 3 \text{ TeV}$  mirrored those used for  $\sqrt{s} = 1.4 \text{ TeV}$ .

Jet finding was performed using the longitudinally invariant  $k_t$  algorithm as described in section 2.4.2. The jet algorithm configuration was optimised using the sensitivity of CLIC to the anomalous gauge couplings using pure signal only, as described in section 2.4.2.1. The optimal jet algorithm configuration for  $\sqrt{s} = 3 \text{ TeV}$  used tight selected PFOs and an R parameter of 1.1. As the cross-section for the  $\gamma\gamma \rightarrow \text{hadrons}$  increases with energy, the effect of these background is more problematic for  $\sqrt{s} = 3 \text{ TeV}$  than for  $\sqrt{s} = 1.4 \text{ TeV}$  [29]. Therefore, it is to be expected that the optimal PFO selection for

Final State	Cross Section [fb]
$e^+e^- \rightarrow \nu\nu qqqq$	71.5
$e^+e^- \rightarrow \nu l qqqq$	106.6
$e^+e^- \rightarrow ll qqqq$	169.3
$e^+e^- \rightarrow qq qq$	546.5
$e^+e^- \rightarrow \nu\nu qq$	1317.5
$e^+e^- \rightarrow \nu l qq$	5560.9
$e^+e^- \rightarrow ll qq$	3319.6
$e^+e^- \rightarrow qq$	2948.9
$e^- \gamma_{\text{EPA}} \rightarrow e^- qq qq$	287.8
$e^- \gamma_{\text{BS}} \rightarrow e^- qq qq$	1268.6
$e^+ \gamma_{\text{EPA}} \rightarrow e^+ qq qq$	287.8
$e^+ \gamma_{\text{BS}} \rightarrow e^+ qq qq$	1267.3
$e^- \gamma_{\text{EPA}} \rightarrow \nu_e qq qq$	54.2
$e^- \gamma_{\text{BS}} \rightarrow \nu_e qq qq$	262.5
$e^+ \gamma_{\text{EPA}} \rightarrow \bar{\nu}_e qq qq$	54.2
$e^+ \gamma_{\text{BS}} \rightarrow \bar{\nu}_e qq qq$	262.3
$\gamma_{\text{EPA}} \gamma_{\text{EPA}} \rightarrow qq qq$	402.7
$\gamma_{\text{EPA}} \gamma_{\text{BS}} \rightarrow qq qq$	2423.1
$\gamma_{\text{BS}} \gamma_{\text{EPA}} \rightarrow qq qq$	2420.6
$\gamma_{\text{BS}} \gamma_{\text{BS}} \rightarrow qq qq$	13050.3

**Table 2.7:** Cross sections of signal and background processes for  $\sqrt{s} = 3$  TeV. In the above table q represents u,  $\bar{u}$ , d,  $\bar{d}$ , s,  $\bar{s}$ , c,  $\bar{c}$ , b or  $\bar{b}$ ; l represents  $e^\pm$ ,  $\mu^\pm$  or  $\tau^\pm$ ; and  $\nu$  represents  $\nu_e$ ,  $\bar{\nu}_e$ ,  $\nu_\mu$ ,  $\bar{\nu}_\mu$ ,  $\nu_\tau$  and  $\bar{\nu}_\tau$ . The EPA and BS subscript on the incoming photon indicates whether the photon is generated from the equivalent photon approximation or beamstrahlung.

$\sqrt{s} = 3$  TeV, tight selected PFOs, is more aggressive at vetoing these backgrounds than for  $\sqrt{s} = 1.4$  TeV, selected PFOs, which is what is observed.

As opposed to training the MVA using 50% of the signal and background events, as was done for the  $\sqrt{s} = 1.4$  TeV analysis, the  $\sqrt{s} = 3$  TeV analysis trained the MVA using 10% of the signal and background events. This modification prevented those events with very large event weights from dominating the  $\chi^2$  fit and producing exaggerated sensitivities. The sensitivity to the anomalous gauge couplings grows with increasing centre of mass energy, therefore, for  $\sqrt{s} = 1.4$  TeV very large event weights were not an

issue. The sample sizes for all signal and background processes was sufficiently large that training on 10% of the total sample was sufficient to achieve good MVA performance. Event selection for the  $\sqrt{s} = 3$  TeV analysis is summarised in table 2.8.

Final State	$\epsilon_{\text{presel}}$	$\epsilon_{\text{BDT}}$	$N_{\text{BDT}}$
$e^+e^- \rightarrow \nu\nu qqqq$	74.4%	46.0%	65,740
$e^+e^- \rightarrow \nu l qqqq$	40.0%	12.0%	25,660
$e^+e^- \rightarrow ll qqqq$	7.5%	1.1%	3,570
$e^+e^- \rightarrow qq qq$	3.7%	0.3%	3,224
$e^+e^- \rightarrow \nu\nu qq$	50.5%	1.2%	30,510
$e^+e^- \rightarrow \nu l qq$	32.0%	0.4%	48,320
$e^+e^- \rightarrow ll qq$	1.4%	-	1,028
$e^+e^- \rightarrow qq$	1.4%	0.1%	3,268
$e^-\gamma_{\text{EPA}} \rightarrow e^- qq qq$	6.6%	0.8%	4,736
$e^-\gamma_{\text{BS}} \rightarrow e^- qq qq$	4.6%	0.7%	13,660
$e^+\gamma_{\text{EPA}} \rightarrow e^+ qq qq$	6.5%	0.8%	4,686
$e^+\gamma_{\text{BS}} \rightarrow e^+ qq qq$	4.7%	0.7%	13,310
$e^-\gamma_{\text{EPA}} \rightarrow \nu_e qq qq$	45.6%	17.2%	18,610
$e^-\gamma_{\text{BS}} \rightarrow \nu_e qq qq$	55.9%	26.7%	110,900
$e^+\gamma_{\text{EPA}} \rightarrow \bar{\nu}_e qq qq$	45.9%	17.3%	18,750
$e^+\gamma_{\text{BS}} \rightarrow \bar{\nu}_e qq qq$	56.5%	27.4%	113,700
$\gamma_{\text{EPA}}\gamma_{\text{EPA}} \rightarrow qq qq$	5.3%	0.7%	5,531
$\gamma_{\text{EPA}}\gamma_{\text{BS}} \rightarrow qq qq$	3.5%	0.4%	16,640
$\gamma_{\text{BS}}\gamma_{\text{EPA}} \rightarrow qq qq$	3.5%	0.4%	15,900
$\gamma_{\text{BS}}\gamma_{\text{BS}} \rightarrow qq qq$	0.6%	-	4,124

**Table 2.8:** Event selection efficiencies for  $\sqrt{s} = 3$  TeV. In the above table,  $\epsilon_{\text{presel}}$  denotes the number of events passing the preselection as a fraction of the total number of events, while  $\epsilon_{\text{BDT}}$  denotes the number of events passing both the preselection and the BDT as a fraction of the total number of events. The EPA and BS subscript on the incoming photon indicates whether the photon is generated from the equivalent photon approximation or beamstrahlung. Entries with a dash indicate an efficiency of less than 0.1%. The event numbers correspond to an integrated luminosity of  $\mathcal{L}_{\text{int}} = 2 \text{ ab}^{-1}$ .

Due to the increased sensitivity of the signal sample, event weights were sampled with greater frequency in the space of  $\alpha_4$  and  $\alpha_5$  for  $\sqrt{s} = 3$  TeV than for  $\sqrt{s} = 1.4$  TeV analysis. Bicubic interpolation was again used to make a continuous surface for the event

weights. These event weight surfaces were then used to construct the  $M_{VV}$  distribution and the  $\chi^2$  surface used to determine the reported sensitivities. Figure 2.17 shows an example of the event weights extracted from the generator and the interpolated surface used to define the  $\chi^2$  surface as a function of  $\alpha_4$  and  $\alpha_5$  for a selected  $\nu\nu qqqq$  event for  $\sqrt{s} = 3$  TeV.

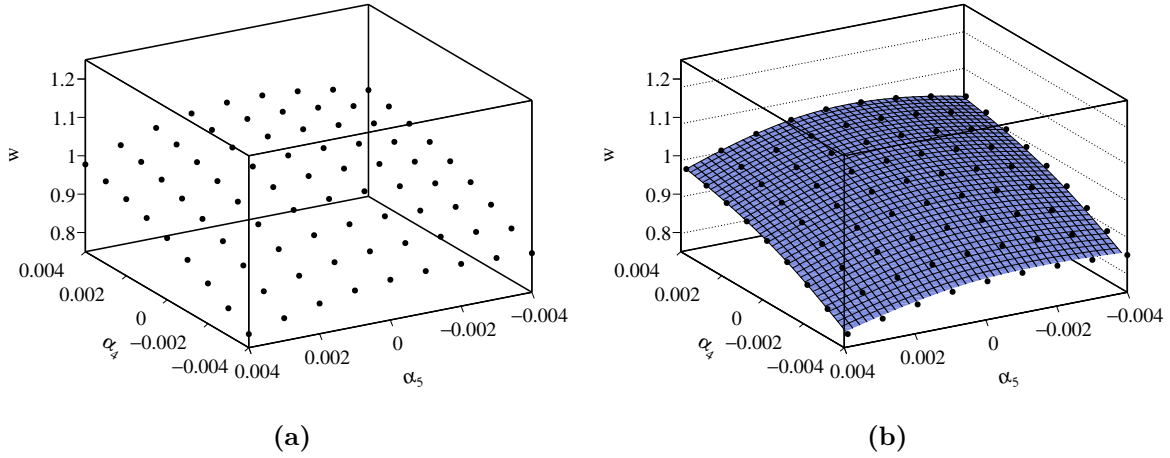


**Figure 2.17:** The event weights,  $w$ , as a function of the anomalous couplings  $\alpha_4$  and  $\alpha_5$  for a selected  $\nu\nu qqqq$  final state events for  $\sqrt{s} = 3$  TeV. These weights are calculated using (a) the generator and (b) bicubic interpolation.

A  $\chi^2$  was applied to the distribution of  $M_{VV}$  to determine the sensitivity of CLIC to the anomalous gauge couplings  $\alpha_4$  and  $\alpha_5$  for  $\sqrt{s} = 3$  TeV. The  $M_{VV}$  distribution used for the fit had an increased number of bins with respect to the  $\sqrt{s} = 1.4$  TeV analysis; the first bin spanned the invariant mass range between 0 GeV and 200 GeV, this was followed by 27 bins of width 100 GeV ranging from 200 GeV to 1300 GeV and finally the last bin contained all invariant masses above 2900 GeV. Figure 2.18 shows the  $M_{VV}$  distribution for signal and background processes for  $\sqrt{s} = 3$  TeV that was used in the  $\chi^2$  fit.

The sensitivity of the CLIC experiment to the anomalous gauge couplings  $\alpha_4$  and  $\alpha_5$  for  $\sqrt{s} = 3$  TeV is shown in figure 2.19a. This result shows the sensitivity after the application of preselection and MVA, described in sections 2.5.1 and 2.5.2, purposed to remove the included background channels. These contours yield the one  $\sigma$  confidence limit on the measurement of

$$-0.0010 < \alpha_4 < 0.0011, \quad (2.13)$$

$$-0.0007 < \alpha_5 < 0.0007. \quad (2.14)$$

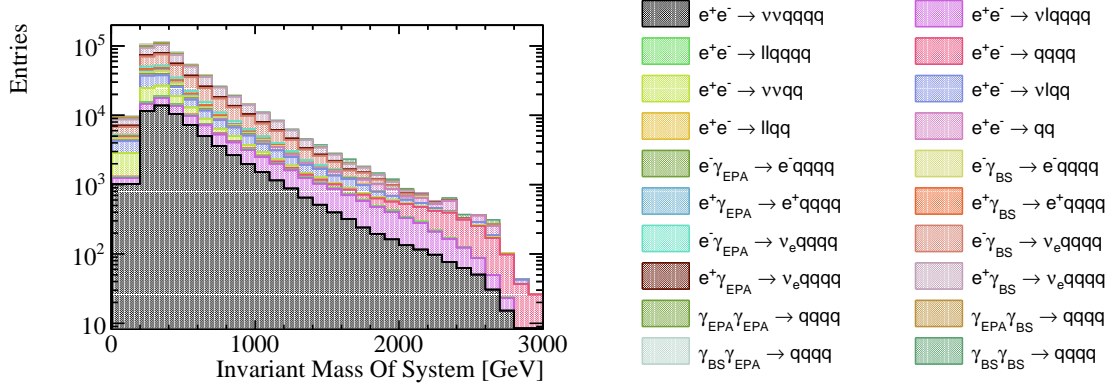


**Figure 2.18:** The distribution of the invariant mass of the system for both signal and background final states that is used in the  $\chi^2$  fit for  $\sqrt{s} = 3$  TeV. The distribution includes effect of event selection and corresponds to an integrated luminosity of  $\mathcal{L}_{int} = 2 \text{ ab}^{-1}$ .

Figure 2.20 shows how the 68% confidence region for the  $\sqrt{s} = 3$  TeV analysis varies with the uncertainty in the cross-section for the signal,  $e^+e^- \rightarrow \nu\nu qqqq$ , and dominant background processes,  $e^\pm \gamma_{BS} \rightarrow \nu_e qqqq$ . These contours were produced using a nuisance parameter as discussed in section 2.7.1. Once again, these systematic uncertainties have a small effect on the reported sensitivity of CLIC to the anomalous gauge couplings due to the shape of the  $M_{VV}$  distribution.

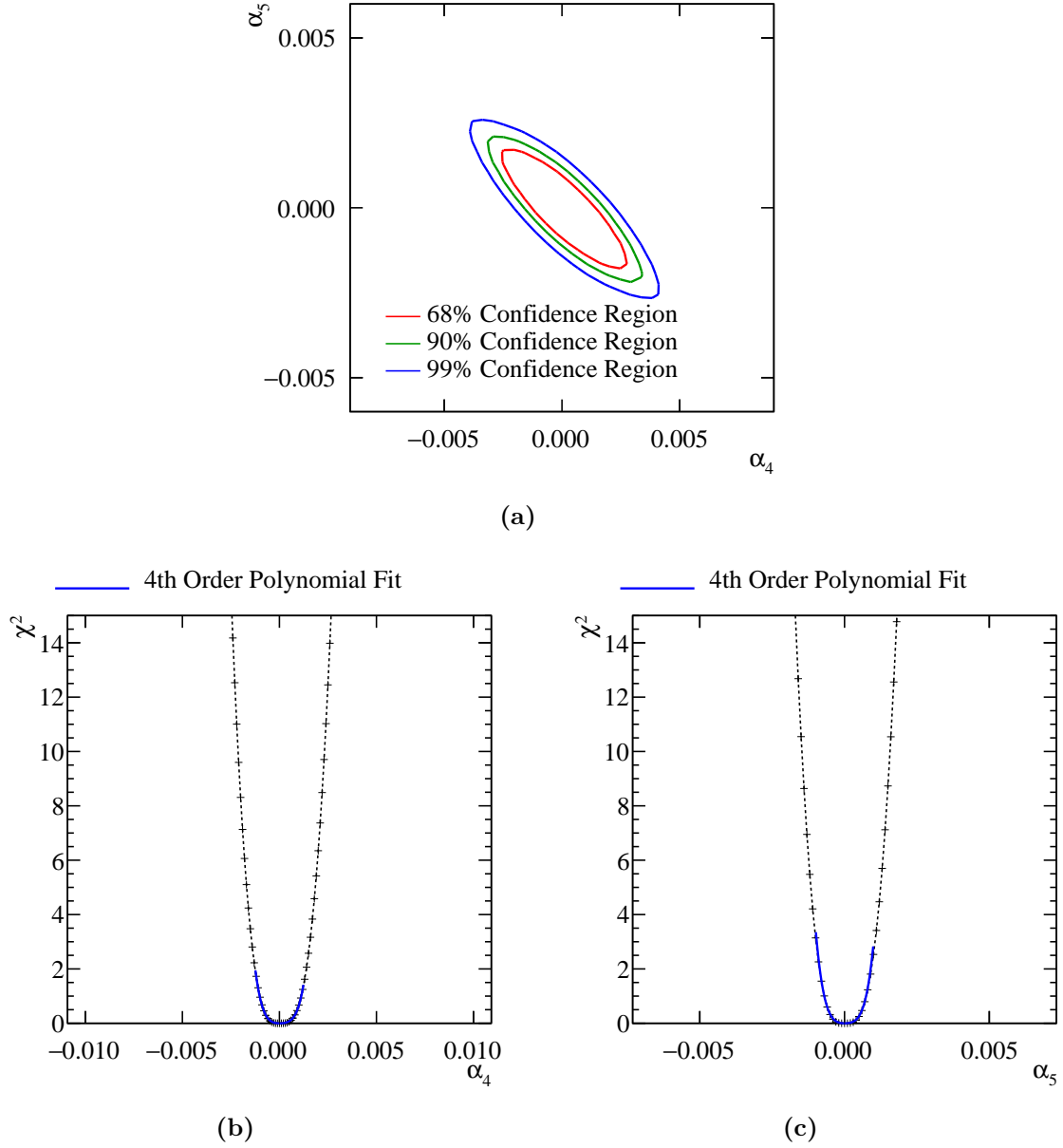


**Figure 2.19:**  $\chi^2$  sensitivity distributions from a fit to  $M_{VV}$  for  $\sqrt{s} = 3$  TeV. Results include the effect of backgrounds after the application of a series of preselection cuts and MVA. (a)  $\chi^2$  sensitivity contours in  $\alpha_4$  and  $\alpha_5$  space. (b)  $\chi^2$  as a function of  $\alpha_4$  assuming  $\alpha_5 = 0$ . (c)  $\chi^2$  as a function of  $\alpha_5$  assuming  $\alpha_4 = 0$ .

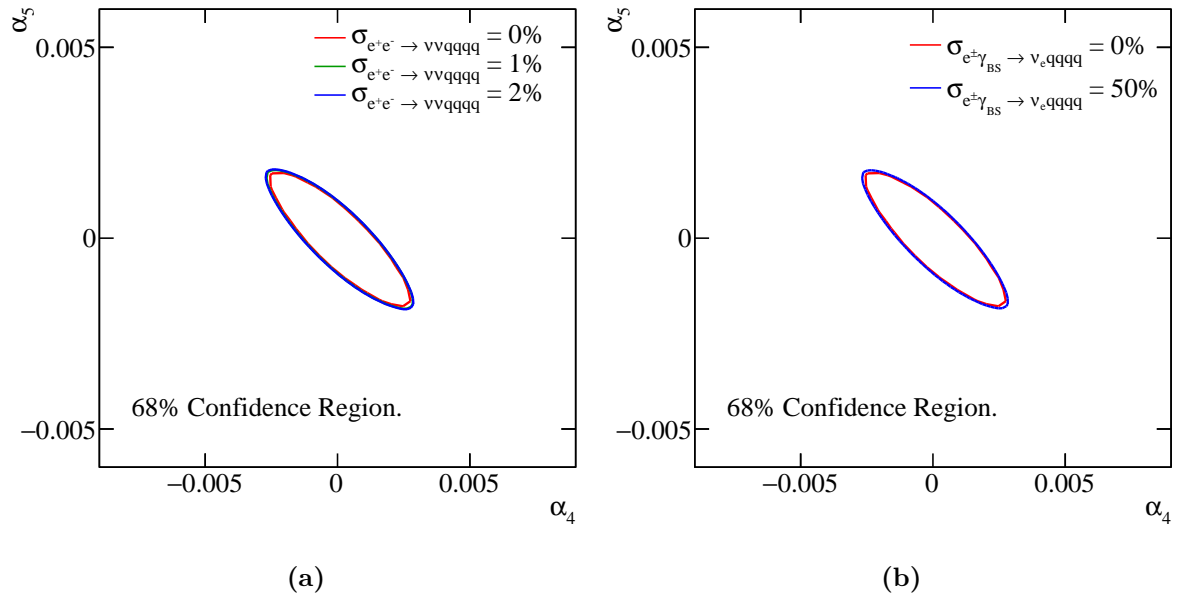


**Figure 2.20:** The 68% confidence region including the effect of uncertainties in the cross-section for (a) the signal process  $e^+e^- \rightarrow \nu\nu qq qq$  and (b) the dominant background processes  $e^\pm \gamma_{BS} \rightarrow \nu_e qq qq$ .



# Colophon

This thesis was made in L<sup>A</sup>T<sub>E</sub>X 2<sub>ε</sub> using the “hepthesis” class [\[34\]](#).



# Bibliography

- [1] David J. Griffiths. *INTRODUCTION TO ELEMENTARY PARTICLES*. 1987.
- [2] Michael E. Peskin and Daniel V. Schroeder. *An Introduction to quantum field theory*. 1995.
- [3] J. Beringer et al. Review of Particle Physics (RPP). *Phys. Rev.*, D86:010001, 2012.
- [4] Steven Weinberg. A Model of Leptons. *Phys. Rev. Lett.*, 19:1264–1266, 1967.
- [5] Jeffrey Goldstone, Abdus Salam, and Steven Weinberg. Broken Symmetries. *Phys. Rev.*, 127:965–970, 1962.
- [6] John Ellis. Higgs Physics. In *Proceedings, 2013 European School of High-Energy Physics (ESHEP 2013): Paradfurdo, Hungary, June 5-18, 2013*, pages 117–168, 2015.
- [7] K. A. Olive et al. Review of Particle Physics. *Chin. Phys.*, C38:090001, 2014.
- [8] R. Keith Ellis, W. James Stirling, and B. R. Webber. QCD and collider physics. *Camb. Monogr. Part. Phys. Nucl. Phys. Cosmol.*, 8:1–435, 1996.
- [9] J. R. Andersen et al. Discovering Technicolor. *Eur. Phys. J. Plus*, 126:81, 2011.
- [10] Christophe Grojean. New approaches to electroweak symmetry breaking. *Phys. Usp.*, 50:1–35, 2007. [Usp. Fiz. Nauk177,3(2007)].
- [11] Celine Degrande, Oscar Eboli, Bastian Feigl, Barbara Jäger, Wolfgang Kilian, Olivier Mattelaer, Michael Rauch, Jürgen Reuter, Marco Sekulla, and Doreen Wackerroth. Monte Carlo tools for studies of non-standard electroweak gauge boson interactions in multi-boson processes: A Snowmass White Paper. In *Proceedings, 2013 Community Summer Study on the Future of U.S. Particle Physics: Snowmass on the Mississippi (CSS2013): Minneapolis, MN, USA, July 29-August 6, 2013*, 2013.
- [12] Christopher Arzt. Reduced effective Lagrangians. *Phys. Lett.*, B342:189–195, 1995.

- [13] Ben Gripaios. Lectures on Effective Field Theory. 2015.
- [14] Maria J. Herrero and Ester Ruiz Morales. The Electroweak chiral Lagrangian as an effective field theory of the standard model with a heavy Higgs. In *Workshop on Electroweak Symmetry Breaking Budapest, Hungary, July 11-13, 1994*, pages 37–54, 1994.
- [15] Anthony C. Longhitano. Low-Energy Impact of a Heavy Higgs Boson Sector. *Nucl. Phys.*, B188:118–154, 1981.
- [16] A. S. Belyaev, Oscar J. P. Eboli, M. C. Gonzalez-Garcia, J. K. Mizukoshi, S. F. Novaes, and I. Zacharov. Strongly interacting vector bosons at the CERN LHC: Quartic anomalous couplings. *Phys. Rev.*, D59:015022, 1999.
- [17] E. Fermi. An attempt of a theory of beta radiation. 1. *Z. Phys.*, 88:161–177, 1934.
- [18] Georges Aad et al. Evidence for Electroweak Production of  $W^\pm W^\pm jj$  in  $pp$  Collisions at  $\sqrt{s} = 8$  TeV with the ATLAS Detector. *Phys. Rev. Lett.*, 113(14):141803, 2014.
- [19] Wolfgang Kilian, Thorsten Ohl, and Jurgen Reuter. WHIZARD: Simulating Multi-Particle Processes at LHC and ILC. *Eur. Phys. J.*, C71:1742, 2011.
- [20] Mauro Moretti, Thorsten Ohl, and Jurgen Reuter. O’Mega: An Optimizing matrix element generator. 2001.
- [21] Torbjorn Sjostrand, Stephen Mrenna, and Peter Z. Skands. PYTHIA 6.4 Physics and Manual. *JHEP*, 05:026, 2006.
- [22] G. Alexander et al. A Comparison of b and u d s quark jets to gluon jets. *Z. Phys.*, C69:543–560, 1996.
- [23] Z. Was. TAUOLA the library for tau lepton decay, and KKMC / KORALB / KORALZ /... status report. *Nucl. Phys. Proc. Suppl.*, 98:96–102, 2001. [96(2000)].
- [24] Toshinori Abe et al. The International Large Detector: Letter of Intent. 2010.
- [25] P. Mora de Freitas and H. Videau. Detector simulation with MOKKA / GEANT4: Present and future. In *Linear colliders. Proceedings, International Workshop on physics and experiments with future electron-positron linear colliders, LCWS 2002, Seogwipo, Jeju Island, Korea, August 26-30, 2002*, pages 623–627, 2002.
- [26] S. Agostinelli et al. GEANT4: A Simulation toolkit. *Nucl. Instrum. Meth.*, A506:250–

- 303, 2003.
- [27] F. Gaede. Marlin and LCCD: Software tools for the ILC. *Nucl. Instrum. Meth.*, A559:177–180, 2006.
  - [28] M. A. Thomson. Particle Flow Calorimetry and the PandoraPFA Algorithm. *Nucl. Instrum. Meth.*, A611:25–40, 2009.
  - [29] J. S. Marshall, A. Münnich, and M. A. Thomson. Performance of Particle Flow Calorimetry at CLIC. *Nucl. Instrum. Meth.*, A700:153–162, 2013.
  - [30] Lucie Linssen, Akiya Miyamoto, Marcel Stanitzki, and Harry Weerts. Physics and Detectors at CLIC: CLIC Conceptual Design Report. 2012.
  - [31] W. Kilian. WHIZARD 1.0: A generic Monte-Carlo integration and event generation package for multi-particle processes.
  - [32] Matteo Cacciari, Gavin P. Salam, and Gregory Soyez. FastJet User Manual. *Eur. Phys. J.*, C72:1896, 2012.
  - [33] Andreas Hoecker, Peter Speckmayer, Joerg Stelzer, Jan Therhaag, Eckhard von Toerne, and Helge Voss. TMVA: Toolkit for Multivariate Data Analysis. *PoS*, ACAT:040, 2007.
  - [34] Andy Buckley. The hepthesis L<sup>A</sup>T<sub>E</sub>X class.